Research Article

Prayoga Wira Adie, Ristiyanto Adiputra*, Aditya Rio Prabowo*, Erwandi Erwandi, Teguh Muttaqie, Nurul Muhayat, and Nurul Huda

Assessment of the OTEC cold water pipe design under bending loading: A benchmarking and parametric study using finite element approach

https://doi.org/10.1515/jmbm-2022-0298 received June 01, 2023; accepted August 08, 2023

Abstract: Ocean thermal energy conversion (OTEC) is a floating platform that generates electricity from seawater heat. The cold water pipe (CWP) used in OTEC has a length of 1,000 m and a diameter of 10 m, making it susceptible to bending loads from ocean currents. To find suitable geometry and material for the CWP, the finite element method was used to model the real-world geometry. In the D/t variation, lower ratios (increased thickness) result in higher critical moments, maximum stress, strain, and displacement. D/t 50 was chosen for the CWP. In the L/D variation, the critical moment's impact on L/D ratio was minimal, while reducing L/D (shorter pipe) increased strain, and larger L/D geometries had higher displacements. L/D 10 was selected as it balanced critical moments and reduced the number of stiffeners needed. For diameter size variation, larger diameters increased critical moment and strain, but smaller diameters (larger L/D ratios) also showed high strain due to necking at two points. A diameter of 12 m was chosen for its exceptionally high critical moment. Steel was selected as the suitable material due to its higher critical moment and maximum stress, despite its higher weight and lower maximum strain than composites. Capital shape imperfections had a minimal effect on the CWP's structure as they were localized.

Keywords: CWP OTEC, buckling propagation, material selection, bending load, finite element method

Prayoga Wira Adie, Nurul Muhayat: Department of Mechanical Engineering, Universitas Sebelas Maret, Surakarta, 57126, Indonesia

1 Introduction

Since the industrial revolution in England in 1760, technological developments have accelerated. However, the industrial revolution led to a large production of greenhouse gases. These greenhouse gases cause global warming. Since the industrial revolution [1], global temperatures have increased by 1° C [2]. The most significant global warming factor is in the energy sector. The energy sector produced 36.44 Giga tons of CO_2 gas equivalent in 2017. Compared to the total CO_2 emissions that year, the energy sector contributed to 71.5% [3]. The energy sources that produce the most significant carbon emissions are petroleum (46% of the total carbon production in the energy sector), natural gas (34% of the total carbon production in the energy sector), and coal (21% of the total carbon production in the energy sector) [4].

Meanwhile, carbon emissions that result from new forms of renewable energy, such as solar, wind, water, and tidal [5-12], are very small [13]. Therefore, there is a need for a transition from fossil to renewable energy so that global warming does not increase. At present, renewable energy in Indonesia is dominated by water energy (19,454 GW), geothermal energy (15,563 GW), and organic fuels (13,562 GW) [14]. Solar energy is also starting to dominate with several research studies involving photovoltaic thermal [15] systems using nanoparticles as the working fluid [16,17], and nanofluid that can absorb more heat, so the photovoltaic panel can be more efficient [18]. Meanwhile, energy originating from the sea is still rarely used (such as ocean wave energy). This is unfortunate because Indonesia is a country dominated by the sea. In research conducted by Alifdini et al., it is known that more than 50%

Erwandi Erwandi, Teguh Muttaqie: Research Center for Hydrodynamics Technology, National Research and Innovation Agency (BRIN), Surabaya 60112, Indonesia

Nurul Huda: National Institute for Aquatic Resources, Technical University of Denmark, Lyngby 2800, Denmark

^{*} Corresponding author: Ristiyanto Adiputra, Research Center for Hydrodynamics Technology, National Research and Innovation Agency (BRIN), Surabaya 60112, Indonesia, e-mail: ristiyanto.adiputra@brin.go.id

^{*} Corresponding author: Aditya Rio Prabowo, Department of Mechanical Engineering, Universitas Sebelas Maret, Surakarta, 57126, Indonesia, e-mail: aditya@ft.uns.ac.id

of the sea waves in South Kuta can be used to generate generators with a capacity of 16.83 MW [19]. This indicates that Indonesia has quite a lot of ocean wave energy potential. Besides ocean wave energy, Indonesia's large oceans also have other renewable energy potentials, namely, ocean thermal energy. The potential for marine thermal energy in Indonesia is quite good. This is because Indonesia has a tropical climate, so the sea temperature in Indonesia does not depend on a particular season or time [20]. Because the potential for marine thermal energy in Indonesia is quite good, this energy should be developed to reduce fossil energy.

Ocean thermal energy can be extracted using the ocean thermal energy conversion (OTEC) technology. This OTEC takes advantage of the difference in the temperature of the hot sea surface and the cold deep seawater. The temperature difference must be more significant than 20°C [21]. OTEC is generally placed on a floating platform like a ship [22]. The thermodynamic cycle in OTEC is the Rankine cycle using ammonia working fluid. The efficiency of the Rankine cycle in OTEC is only 6-7% [23]. Cold deep seawater is pumped to the platform using a cold water pipe (CWP). CWP on OTEC usually has a diameter of 10 m, is 0.1 m thick, and is 1,000 m long. This is because the cold water must still be cold when it reaches the platform, so a larger pipe means reduced heat transfer from the outside pipe [24]. The distance between the stiffeners on the CWP is 100 m [25]. In the CWP, several loads cause failure in the CWP. The load is a bending load due to seawater currents and hydrostatic pressure. However, this study will discuss the CWP when subjected to bending loads because the distance between the stiffeners at the CWP is large, causing this pipe to fail quickly due to twisting.

In the studies that have been carried out, research on CWP focuses on its stability. An example of research conducted by Adiputra and Utsunomiya was regarding the strength of several materials for CWP OTEC [26]. In addition, research that examines pipes under bending loads focuses on their geometry. An example of research conducted by Yudo and Yoshikawa was discussing pipes with various D/t and L/D ratios at bending loads [27]. Therefore, this study investigates geometries with large dimensions and materials capable of withstanding bending loads to obtain a CWP OTEC design with high bending strength (as a result, thermodynamics of the pipe is not being analyzed). Furthermore, this study examines the materials commonly used in the maritime industry when subjected to bending loads to determine suitable materials for CWP OTEC.

2 Buckling on structure and infrastructure

In a structure, failure occurs when it can no longer sustain the applied load. Failures can take various forms, such as vielding, fatigue, and buckling [28]. In the context of material and structural mechanics, yielding failure happens when a material undergoes permanent plastic deformation due to stress exceeding the material's elastic limit. Fatigue failure occurs when a material or structure experiences damage or failure as a result of repeated or cyclic loading over an extended period [29]. Buckling is a failure where a structure fails to maintain its position. The focus of this study is buckling failure (because pure bending makes this failure). Buckling can occur in all structures that experience axial compression loads and bending loads [30]. An example of a pipe experiencing buckling failure can be seen in Figure 1. Figure 1 shows the pipe's buckling failure due to axial compression loads. This buckling failure does not only occur in the pipe structure. Other structures, such as cemented I-beam structures, can also experience this failure. Figure 2 is an I-beam structure that is given cement, which has failed buckling due to bending loads.

As a result of the buckling in the I-beam (in Figure 2), the cement that is cast on it breaks due to the brittle nature of the cement [33]. This failure does not only occur in large structures. The frame on the car can also experience buckling when exposed to heavy loads. An example of buckling is shown in Figure 3, in which a wheel coupler formwork support component is subjected to bending loads.

In Figure 3, it can be seen that the buckling is in the middle of the specimen. This is because the load given to



Figure 1: Buckling on pipe [31].

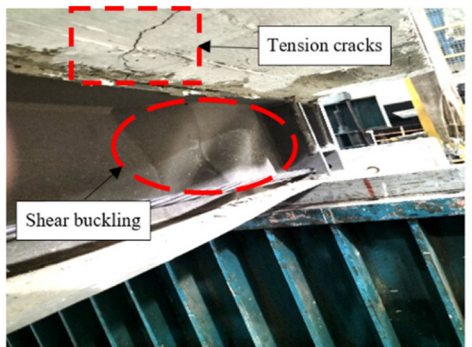




Figure 2: I-beam structure experiencing buckling failure [32].

the specimen is in the middle of the specimen. Apart from compression and bending loads, buckling can also occur due to external hydrostatic pressure around it [35]. This failure usually occurs in pipes under the sea/offshore pipes. An example of a pipe that is buckling due to external hydrostatic pressure can be seen in Figure 4.

3 Buckling phenomenon analytic concept

The researchers who investigated buckling phenomenon were Tymoshenko and Gere [36], who focused on axial compression loads. They found that a long pipe's critical stress on both ends is suspended, as shown in the following Eq. (1) [36]:

$$\sigma_{\rm cr} = \frac{Et}{r\sqrt{3(1-v^2)}},\tag{1}$$

where σ_{cr} is the critical stress, *E* is Young's modulus, *t* is the thickness of the pipe, r is the pipe's radius, and v is Poisson's ratio.

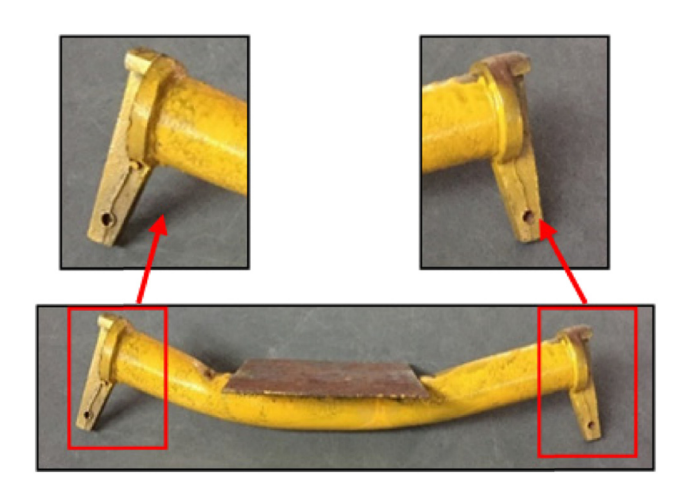


Figure 3: Buckling on the wheel coupler formwork support [34].

For a cylindrical pipe with a thin wall subjected to a bending moment load, the maximum stress equation can be seen in the following equation [37]:

$$\sigma = \frac{M}{\pi r^2 t},\tag{2}$$

where σ is the maximum stress in the axial direction, and M is the bending moment load.

If it is assumed that a pipe with a thin pipe wall is loaded with buckle bending when the compression stress reaches a value where the stress reaches buckling failure, then the critical moment can be found by combining Eqs. (1) and (2). If it is assumed that the material used is steel with a Poisson ratio of 0.3, then the following equation [37] is obtained:

$$M_{\rm cr} = \sigma_{\rm cr} \pi r^2 t = 0.605 \pi E r^2 t,$$
 (3)

In the previous studies that examined circular pipes under bending loads, such as Chwalla [38] and Brazier [39], it was found that the results of their research had a range of values between 0.55 and 1.3 values, which were formulated in Eq. (3). In the study conducted by Chwalla, the critical moment formula can be seen in the following equation [38]:

$$M_{\rm cr} = 0.378\pi E r^2 t.$$
 (4)

Meanwhile, Brazier found that the critical moment formula can be seen in the following equation [39]:

$$M_{\rm cr} = 0.33\pi E r^2 t. \tag{5}$$

Eq. (3) can reference the value of the critical moment. However, the actual value of a pipe cannot be calculated using Eq. (3). This is because the critical moment is greatly influenced by other parameters, especially the D/t ratio [37]. Eq. (6) [40] can be used to find the buckling moment in the plastic area.

$$M_{\rm p} = \left(1.05 - 0.0015 \frac{D}{t}\right) \sigma_{\rm Y} D^2 t. \tag{6}$$



Figure 4: Pipeline failure due to external hydrostatic pressure.

Where D is the diameter of the pipe and σ_y is the yield stress. This equation is broadly acknowledged to be a good design criterion.

In Eqs. (3)–(6), several factors can affect the magnitude of the critical moment in a cylindrical structure. Young's modulus (E) and yield stress influence the magnitude of the critical moment in the material forming the structure. At the same time, the diameter/radius and thickness affect a system's essential moment in the structure's geometry. Therefore, the parameters used in this research for CWP OTEC are material, diameter size, and diameter/thickness ratio (D/t).

Another phenomenon that exists in a pipe that is given by the bending load is ovality. This phenomenon causes the surface area of the originally circular pipe to become oval in shape. A schematic of the oval deformation can be seen in Figure 1(a). Longitudinally, the pipe will experience curvature, and a schematic of the curvature can be seen in Figure 1(b).

In Figure 5, the part that comes out of the circle is called outward buckling, and the part that goes into the circle is called inward buckling. Ovalization has a nonlinear moment–curvature relationship as its main effect, represented in the following equation [43]:

$$M = EI(M) \frac{\mathrm{d}^2 u}{\mathrm{d} x^2},\tag{7}$$

where I is the moment of inertia, M is the applied bending load, and (d^2u/dx^2) is the curvature [43]. The curvature itself can also be known by the amount of rotational displacement divided by the distance between the stiffeners of the structure. Therefore, the distance between the stiffeners/diameter (L/D) ratio is also included in the variation in this study.

4 Research milestones

Several studies have been conducted on pipes subjected to bending loads. Kyriakides *et al.* [44] wrote about buckling localization and propagation under bending loads, and Dimopoulos and Gantes [45] studied buckling in cylindrical shell wind turbine towers. Ghazijahani and Showkati [46] investigated cylindrical shells under bending and external loads. Karampour and Albermani [47] investigated clasp interactions in textured deep underwater pipelines. In the same year, Yudo and Yoshikawa [48] investigated the buckling phenomenon for imperfect pipes under pure bending loads. In addition, in the same year, Winkler *et al.* [49] wrote about the fatigue behavior of high-strength steel mono strands under bending loads. Li *et al.* [50] investigated the performance of concrete-filled double skin steel tube (CFDST) beams using high-

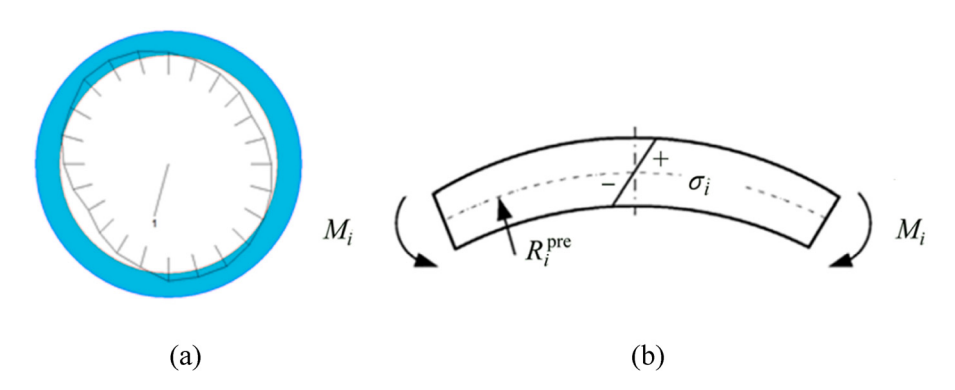


Figure 5: Analytical concept in this study: (a) oval deformation [41] and (b) curvature [42].

strength steel under bending loads, and in the same year, Kim et al. [51] wrote about the strength of CFDST members with shear connectors under bending loads. Yuan et al. [52] investigated the buckling of bi-material pipes under bending loads. For updates from each study conducted, see Table 1.

From the existing research milestones, it can be seen that research on CWP for OTEC has never been carried out. This is because the geometry of the CWP is extreme, and OTEC itself is still not popular. Therefore, this research was conducted to find suitable geometries and materials for CWP OTEC.

Table 1: Summarized reference of the milestone study

Year	Authors	Subject	Concluding Remarks
2008	Stelios Kyriakides, Ali Ok, and Edmundo Corona	Localization and propagation of buckling under bending loads in steel tubes	The relationship between the given moment load and the pipe curvature that occurs can be seen [44]
2012	C.A. Dimopoulos and C.J. Gantes	Experimental investigation of wind turbine tower cylindrical shell buckling	The result of this study is that imperfections affect the failure of the windmill poles. However, the holes in the poles do not have a major effect on the failure of the windmill poles [45]
2013	Tohid Ghanbari Ghazijahani and Hossein Showkati.	Experiments on cylindrical shells under bending loads and external stresses	In pure bending loads, when the location of the load application (concentrated load) moves from the stress zone of the section to the neutral axis, the behavior of the protrusion of the section changes to flattening [46]
2015	Hassan Karampour and Faris Albermani	Clasp interactions in a textured deep underwater pipeline	Textured pipes have a better buckling propagation compared to cylindrical pipes. However, cylindrical pipes are more sensitive to imperfections than textured pipes [47]
2015	Hartono Yudo and Takao Yoshikawa	The buckling phenomenon for imperfect pipes under pure bending	A parameter $\beta = (D/t)(\sigma_Y/E)$ can be a parameter of the yielding effect on the buckling moment. If β is large, then the pipe will experience elastic buckling. If it is small, then the pipe will experience plastic buckling [48]
2015	Jan Winkler, Christos T. Georgakis, and Gregor Fischer	Fatigue behavior of high- strength steel mono strands under bending loads	The research experiment results show that the interwire movement due to transverse deformation is highest on the neutral axis of the mono strand [49]
2019	Ali Binazir, Hassan Karampoura, Adam J. Sadowski, and B. P. Gilbert	Pure bending loading in a pipe- in-pipe system	The strength of the pipe system inside the pipe is influenced by the ratio of the outer pipe thickness to the inner pipe thickness [53]
2021	Wei Li, Wei-Jie Li, Li-Feng Xu, and Fa-Cheng Wang	CFDST beam performance using high-strength steel under bending loads	HSS is more brittle at bending loads than ordinary steel when used as a sandwich material wall [50]
2021	Seung-Eock Kim, George Papazafeiropoulos, Viet- Hung Truong, Phu-Cuong Nguyen, Zhengyi Kong, Nguyen-Th^e Duong, Van-Trung Pham, and Quang- Viet Vu	Strength of CFDST members with shear connectors under bending loads	The ratio of outside diameter to inside diameter, outer diameter to outside thickness, inside diameter to inside thickness, and outside thickness to inside thickness affects the bending strength of the material [51]
2022	Lin Yuan, Jiasheng Zhou, Haowei Liu, and Nian- Zhong Chen	Buckling of the bi-material pipe under bending loads	The range where buckling occurs can be checked. Checking this range by looking at the minor buckling that arises due to the bending load [52]

5 Methodology

The method used in this study was the finite element method (FEM). The FEM is a numerical technique that models a structure by dividing it into small elements (mesh). After meshing, interactions were defined at certain points (nodes) between these elements. Then, calculations were made at each node using predetermined mathematical equations [54]. This method was used in this study because it helped to reduce the costs required for the research. Moreover, using this method allowed for the use of numerous variations in the analysis [55].

5.1 Numerical validation

The validation carried out for this study was by replicating the research conducted by Yadav and Gerasimidis [56] regarding the instability of the cylindrical shell under bending loads. In the research conducted by Yadav and Gerasimidis, a cantilever pipe was subjected to a bending load at its end. This issue is similar to the problem present in CWP OTEC, where CWP OTEC is a cantilever pipe with a free end, resulting in a bending load. Furthermore, the research conducted by Yadav and Gerasimidis already has complete information, making it easy to replicate.

The geometry used by Yadav and Gerasimidis is a cylindrical shell with a distance between stiffeners of 20 m, a radius of 4 m, a radius/thickness ratio (R/t) of 60,

and a modal shape imperfection with a magnitude of 0.1. The geometry of the validation carried out can be seen in Figure 6.

The material used was medium carbon steel with a yield stress of 355 MPa, Young's modulus of 210 GPa, and Poisson's ratio of 0.3. For material input, Yadav and Gerasimidis 2019 used the Ramberg–Osgood plasticity model. For the equation of plasticity, Ramberg–Osgood can be seen in the following equation [44]:

$$\varepsilon = \frac{\sigma}{E} \left[1 + \frac{3}{7} \left(\frac{\sigma}{\sigma_y} \right)^{n-1} \right]. \tag{8}$$

The boundary conditions used also followed a study conducted by Yadav and Gerasimidis [56]. Fixed ends are made on one side of the pipe, so U1 = U2 = U3 = UR1 = UR2 = UR3 = 0. Meanwhile, on the other hand, it is a given moment load. The given moment is a rotational displacement using θ . The boundary conditions for the validation carried out can be seen in Figure 7.

Validation was carried out using ABAQUS software using the static risk method. The result of the moment load will be normalized by $M = D^2t\sigma_y$, and the curvature will be normalized with $=\frac{t}{D^2}$, where D is the pipe diameter, t is the pipe thickness, and the yield strength. The results of the numerical validation can be seen in Table 2 and Figure 8.

From the results obtained (in Table 2 and Figure 8), it can be seen that the difference between the study



Figure 6: Geometry for validation (in mm).

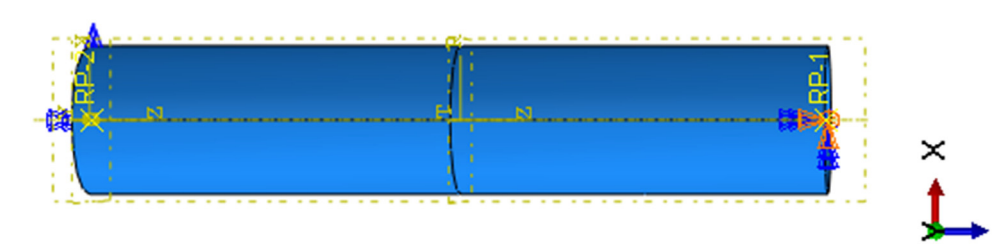


Figure 7: Boundary condition for validation.

Table 2: Validation result

Normalized moment	Normalized curvature
0.952	0.88
0.985	1.01
3.5	15
	moment 0.952 0.985

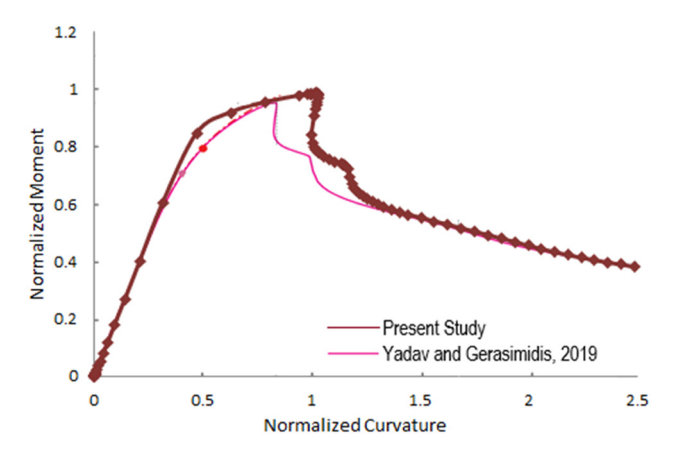


Figure 8: Moment-curvature curve, and thus validation result.

conducted by Yadav and Gerasimidis in 2019 and the current study at critical moments is similar, with only about a 3.5% difference. However, the curvature at the critical moment has a difference of 15%. This is due to the differences in the input material, especially when it reaches its yield strength. In this study, the ductility criteria used were the same as those used in bilinear materials, where the boundary between elastic and plastic behavior forms a

single point. On the other hand, in the study conducted by Yadav and Gerasimidis, the ductility criteria used involved the actual stress–strain curve, and thus, they did not form a single point at the boundary between elastic and plastic behavior. This is due to the limitation in the ABAQUS CAE software, which does not allow the direct input of the actual stress–strain curve at the yield strength.

5.2 Mesh convergence study

The mesh convergence study was conducted using a model replicated from a study conducted by Yadav and Gerasimidis [56]. The geometry, materials, and boundary conditions were identical to those in the previous validation. The elements used for this research were shell elements. This is because the geometry used for this research was a cylindrical shell, and using shell elements can optimize the numerical calculations performed. For the mesh convergence study, ABAQUS software used the linear buckle method to make the results obtained more linear. The varied mesh started from the mesh with the largest size of 200 mm and the smallest size obtained when it was converged. The results of the conducted mesh convergence study can be seen in Figure 9.

Figure 9 shows that the greater the number of elements used, the more convergent the results obtained. When the number of elements was added, the critical moment obtained differed from the number of fewer elements. Figure 9 adds a straight line to the graph to see where the convergence occurred. From the figure, it can be seen that a mesh size of 55 mm was a good mesh size to use. It was shown that with the 55 mm mesh size, the critical moment results obtained were similar to the smaller

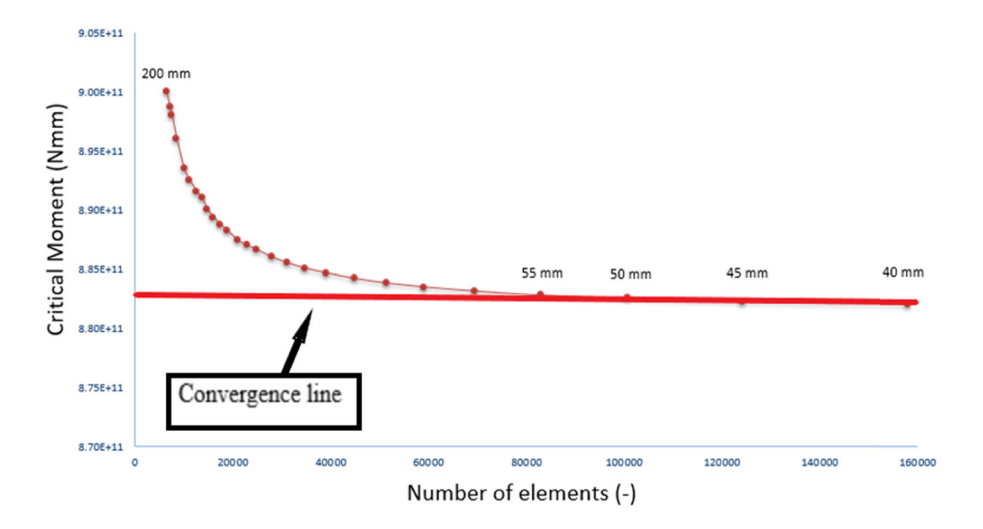


Figure 9: Results from a mesh convergence study.

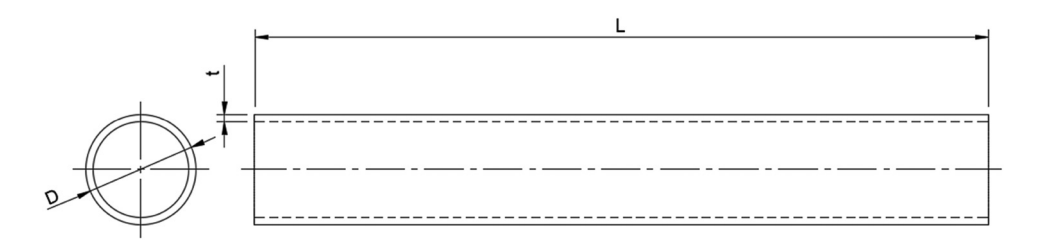


Figure 10: Geometry modeling

mesh size. In addition, a larger mesh size can also reduce the number of elements used in numerical calculations so that it was more efficient in numerical calculations.

5.3 Numerical modeling

The numerical modeling for CWP OTEC used in this study was to model it on a cylindrical shell. This was used so that the numerical calculations were not too complicated and that the numerical calculations can be efficient. This geometry can also effectively represent CWP OTEC because CWP OTEC is a thin-walled cylindrical pipe. The shape of the geometry used in this study can be seen in Figure 10, in which the diameter (*D*), thickness (*t*), and distance between stiffeners (*L*) valued for each variation vary, depending on the variation used. The variations used can be seen in the following section.

The material properties input into ABAQUS CAE included Poisson's ratio, Young's modulus, yield stress, and plasticity properties in the material model used. These properties are influential in calculating the critical moment of a cylindrical shell pipe subjected to bending loads, as described in Eqs. (3) and (6).

5.4 Geometry variation

There were four geometric variations used in this study. The first variation was the diameter/thickness ratio (D/t), then the distance between stiffeners/diameter ratio (L/D), the variation in the size of the diameter used, and the imperfection variation. In the geometric variations, the material used was the same for each variation, namely, carbon steel with moderate plasticity Ramberg–Osgood whose similarities can be seen in Eq. (8) [44].

5.4.1 D/t variation

The variation of D/t was studied due to the thin thickness of CWP OTEC. Additionally, the D/t ratio of the cylindrical shell

structure affected the magnitude of its critical moment. For the D/t variation, a fixed diameter and a fixed distance between stiffeners were used, but for a different thickness. The variation of D/t used can be seen in Table 3.

5.4.2 L/D variation

The variation of L/D was used in this research because this variation affected the number of stiffeners to be used in CWP OTEC. Thus, in this variation, we seeked options with good structural strength and more efficient use of stiffeners. For the L/D variation, the diameter and thickness used were the same, but the distance between the stiffeners of the pipe to be simulated was different. The variation of L/D used can be seen in Table 4.

5.4.3 Diameter size variation

Due to manufacturing limitations in CWP OTEC caused by its large size, we attempted to reduce the diameter to investigate the effects. However, reducing the diameter increased the

Table 3: D/t variation

Code	D/t	L/D	D (mm)	t (mm)	<i>L</i> (mm)
A-1	100	11.11	9,000	90	100,000
A-2	150	11.11	9,000	60	100,000
A-3	200	11.11	9,000	45	100,000
A-4	250	11.11	9,000	36	100,000
A-5	300	11.11	9,000	30	100,000

Table 4: L/D variation

Code	D/t	L/D	D (mm)	t (mm)	L (mm)
B-1	100	2.5	10,000	100	25,000
B-2	100	5	10,000	100	50,000
B-3	100	7.5	10,000	100	75,000
B-4	100	10	10,000	100	100,000

to resist bending loads so that failure was not easy. Therefore,

Table 5: Diameter variation

Code	D/t	L/D	D (mm)	t (mm)	L (mm)
C-1	100	33.33	3,000	30	100,000
C-2	100	16.67	6,000	60	100,000
C-3	100	11.11	9,000	90	100,000
C-4	100	8.33	12,000	120	100,000

number of CWPs used in OTEC. Variations in diameter, the distance between stiffeners, and the D/t ratio were the same, so the difference was in the diameter and thickness used. The variations in the diameter used can be seen in Table 5.

5.4.4 Imperfection variation

The last geometric variation was the imperfection variation. In this variation, this study investigated how imperfections affected the structural strength of CWP OTEC. The imperfection used was a modal shape imperfection, where the imperfection value was obtained by multiplying the results from the eigenvalue analysis with the specified magnitude value. For imperfection, variations can be seen in Table 6.

5.4.5 Material variation

The material used in this study needed to be varied to find a good material for CWP OTEC. The selected material had

Table 6: Imperfection variation

Code	Imperfection (W_0/t)	D (mm)	t (mm)	<i>L</i> (mm)
E-1	0.05	9,000	90	100,000
E-2	0.1	9,000	90	100,000
E-3	0.15	9,000	90	100,000
E-4	0.2	9,000	90	100,000
E-5	0.25	9,000	90	100,000
E-6	0.5	9,000	90	100,000
E-7	0.75	9,000	90	100,000
E-8	1	9,000	90	100,000

steel, aluminum, and two types of fiber-reinforced plastic (FRP [57]) were used in this study. The materials were chosen because they were corrosion-resistant. Therefore, they can be applied to CWP OTEC due to the corrosive nature of the CWP OTEC environment. High-density polyethene (HDPE) is also a material that can be used for CWP OTEC. However, HDPE material cannot be used on pipe sizes above 1.6 m in diameter. For materials that had a significant weight, a floater was provided. In material variations, the variable geometry was all fixed. The materials used in this study can be seen in Table 7.

In this study, several materials used Ramberg–Osgood's

In this study, several materials used Ramberg–Osgood's plasticity. For iron, the Ramberg–Osgood equation from Eq. (8) was used with an *n*-value of 9 [44]. In composites, the Ramberg–Osgood equation used was the Ramberg–Osgood equation for FRP, which can be seen in the following Eq. (9) [61]:

$$\sigma = \frac{E_0 \varepsilon}{\left(1 + \left(\frac{E_0 \varepsilon}{\sigma_0}\right)^n\right)^{1/n}},\tag{9}$$

where σ is the stress, E_0 is the initial modulus, σ_0 is the asymptotic stress level, and ε is the strain. For CFRP material, the E_0 value is 138 GPa, σ_0 value is 100 GPa, and n is 10. Meanwhile, for GFRP, the E_0 value is 45.6 GPa, σ_0 is 100 GPa, and n is 10 [62].

5.5 Geometry/material selection

The selection of geometry/material for CWP OTEC was based on various factors, including critical moment, maximum stress, maximum strain, maximum displacement, and other relevant parameters that differed for each variation. High critical moments were chosen from each variation to ensure that CWP OTEC can withstand significant bending. The consideration of maximum stress and strain was also crucial in the selection of geometry/material to ensure that they can endure high stress and strain. Additionally, the largest displacement was preferred so that the pipe structure can undergo substantial displacement before failure occurred.

Table 7: Material variation

Code	Material	Modulus Young (GPa)	Yield strength (MPa)	Density (kg/m³)	Plasticity	D (mm)	t (mm)	L (mm)
D-1	Steel [44]	210	455	7,840	Ramberg-Osgood	9,000	90	100,000
D-2	Al 6061T6 [58]	68.9	276	2,700	Bilinear	9,000	90	100,000
D-4	CFRP [59]	130	1,756	1,800	Ramberg-Osgood	9,000	90	100,000
D-5	GFRP [60]	45.6	1,280	2,500	Ramberg–Osgood	9,000	90	100,000

In addition to the aforementioned factors, the selection of material/geometry is also based on the characteristics of each variation. For the D/t variation, the geometry's volume is considered as it can affect the total weight of the structure. In the L/D variation, the required number of stiffeners is also determined since a smaller distance between stiffeners results in a greater total number of stiffeners used. When considering material variations, the material's density is also considered when selecting materials for CWP OTEC. This is because density also influences the total weight of the CWP OTEC structure.

6 Results and discussion

The results and discussion section analyzes the effects of the applied variations on a pipe structure subjected to bending loads. The parameters under observation include critical moment, maximum stress, maximum strain, and maximum displacement for each variation. Subsequently, conclusions regarding the appropriate geometry/material for CWP OTEC will be drawn based on the considerations explained in the methodology.

6.1 D/t variation

The results of this variation were compared in the form of a moment *versus* curvature graph, which can be seen in

Figure 11. The graph shown in Figure 11 shows that as the thickness increased (or the D/t ratio decreases), the critical moment also increased. This was because the moment of inertia of the geometry with a larger thickness was higher, allowing it to withstand higher bending stresses. The formula for the area moment of inertia for a hollow cylinder can be seen in Eq. (10) [63].

$$I = \frac{\pi}{64}(D^4 - d^4),\tag{10}$$

where I is the area moment of inertia, D is the outside diameter of the cylinder, and d is the inside diameter of the cylinder. The graph in Figure 11 shows that the plastic deformation region in geometries with higher thickness was larger compared to geometries with lower thickness. This was because increasing the thickness of a structure can enlarge the area capable of undergoing plastic deformation. But apart from the moment–curvature graph, in the geometry selection, it was also necessary to know the contours of the specimen to find out where the failure occurred. The stress contour can be seen in Figure 12, the strain contour in Figure 13, and the displacement contour in Figure 14.

In Figure 12(a), it shows the stress contours of geometry A-1 when elastic (moment of 2.72×10^{10} Nmm), after yielding (moment of 2.57×10^{12} Nmm), and at the critical moment (moment of 2.68×10^{12} Nmm). In Figure 12(b), it displays the stress contours of geometry A-3 when elastic (moment of 1.36×10^{10} Nmm), during plastic deformation (moment of 1.07×10^{12} Nmm), and at the critical moment (moment of 1.07×10^{12} Nmm). Lastly, in Figure 12(c), it depicts the stress

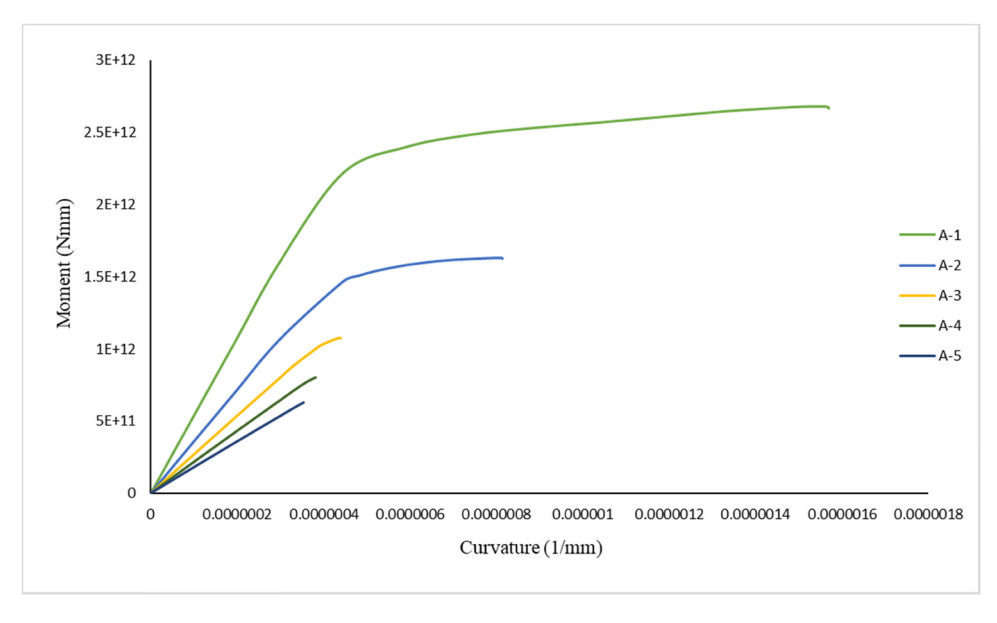


Figure 11: Moment-curvature graph for D/t variation.

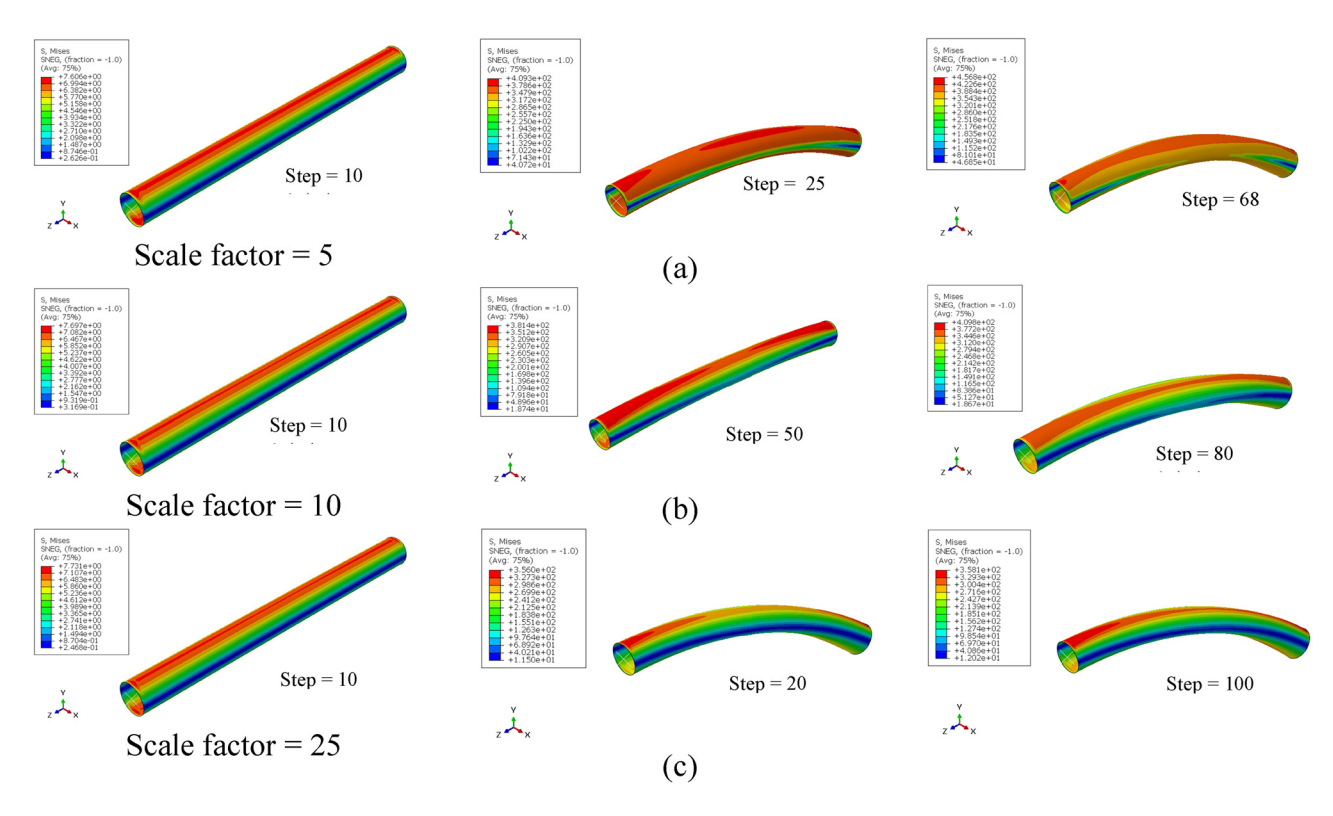


Figure 12: Stress contours: (a) A-1, (b) A-3, and (c) A-5.

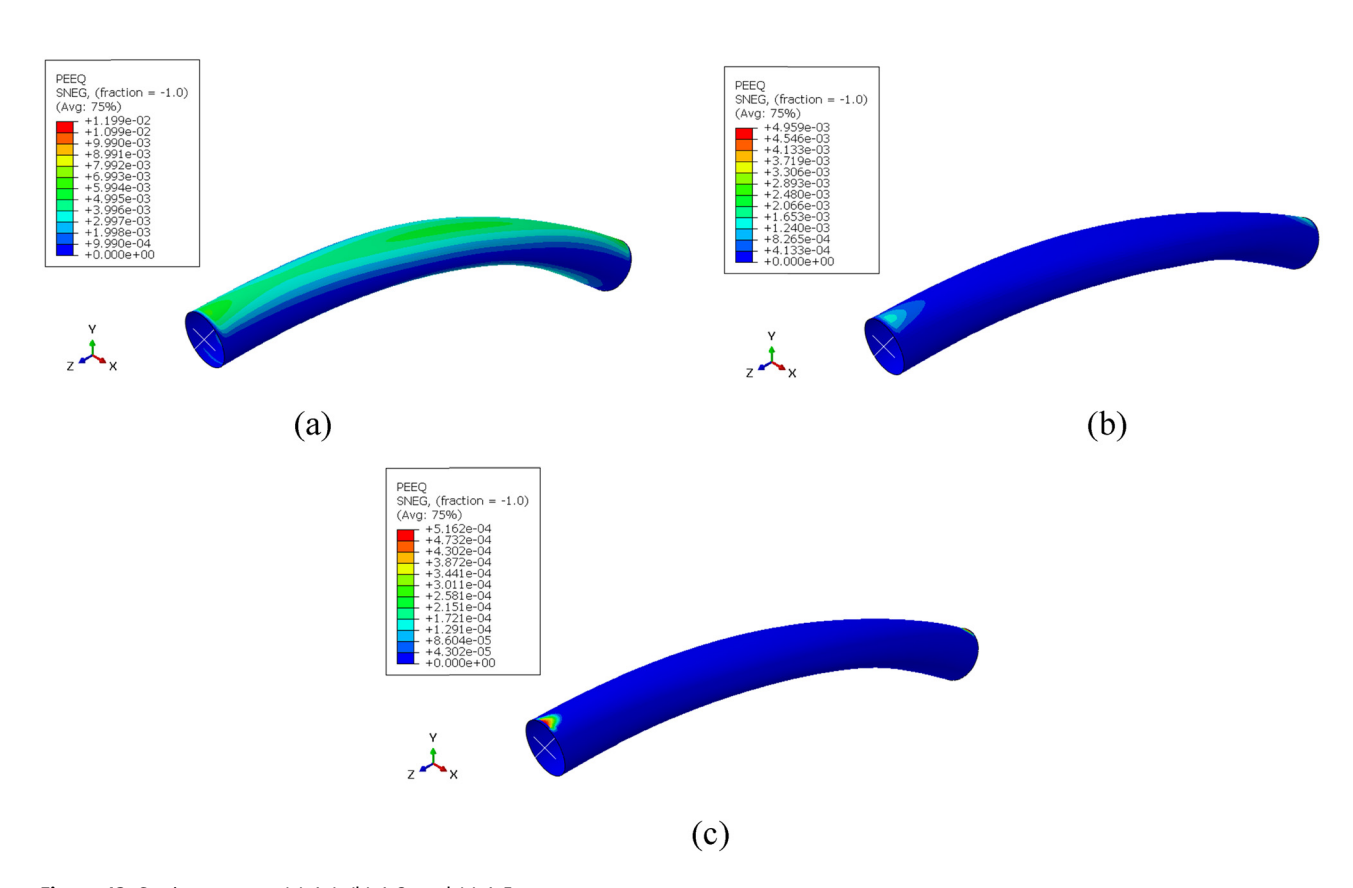


Figure 13: Strain contours: (a) A-1, (b) A-3, and (c) A-5.

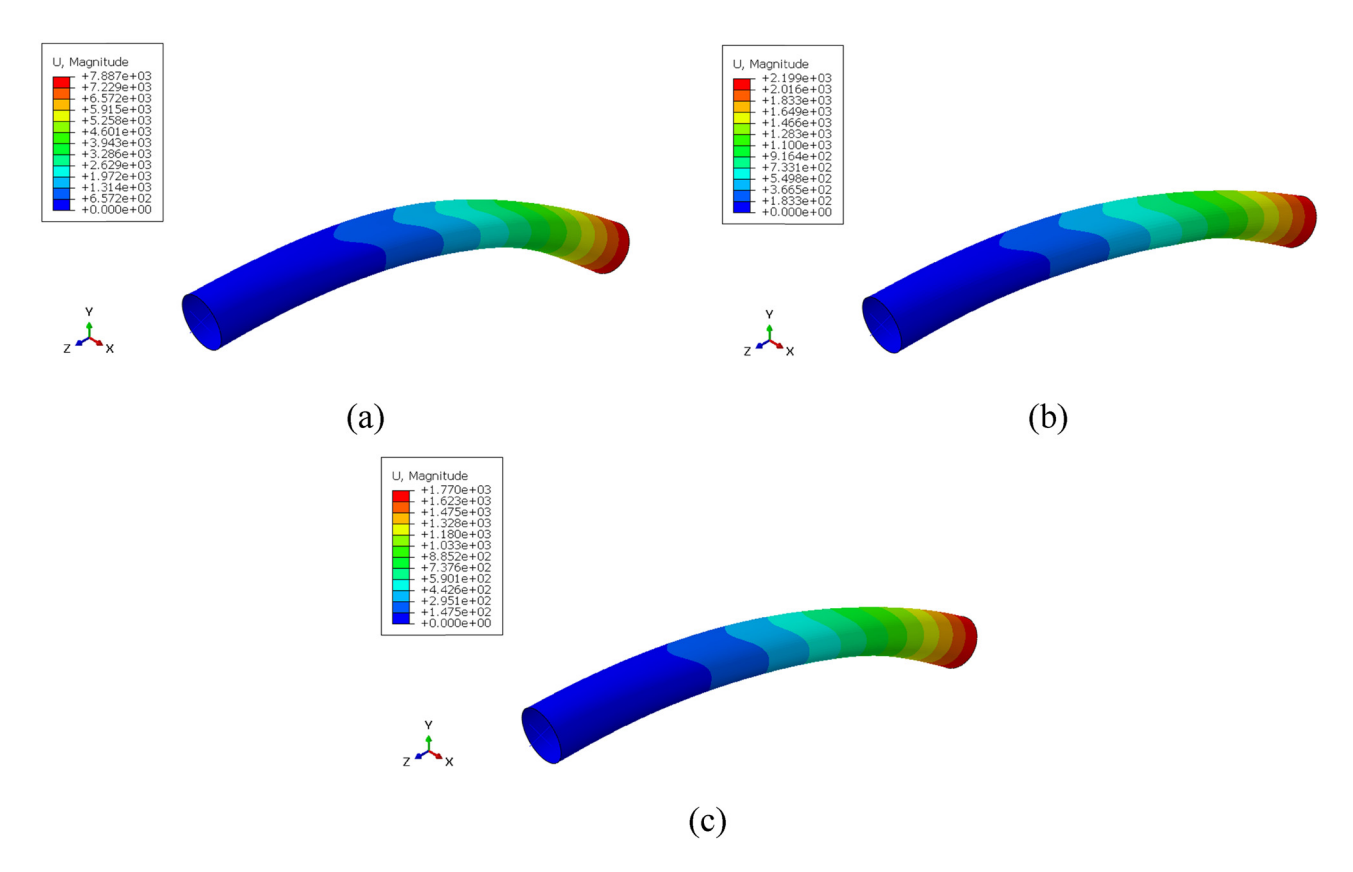


Figure 14: Displacement contours: (a) A-1, (b) A-3, and (c) A-5.

contours of geometry A-5 when elastic (moment of 9.05×10^9 Nmm), during plastic deformation (moment of 5.27×10^{11} Nmm), and at its critical moment (moment of 6.25×10^{11} Nmm).

By observing the critical stresses (in Figure 12), it can be noted that the larger the thickness (the smaller the D/t ratio), the higher the critical stress. This was also due to the larger moment of inertia of geometries with greater thickness, allowing them to withstand higher bending stresses (as in Eq. (10)). Figure 12(a)–(c) shows that the maximum stress at the top of the pipe moved toward the pipe's ends, while at the bottom, it moved toward the center. This was because of the nature of bending stress, where one part of the object experienced tensile stress while the opposing part experienced compressive stress.

In the strain contours (Figure 13), it can be observed that the larger the thickness, the higher the strain that appears. This was because strain and stress were directly related, where higher stress led to higher strain. The locations where strain occurred were also the same as where stress occurred. For example, in Figure 12(c), the maximum stress occurred at the ends of the pipe (when viewed from the top), and if compared to the strain that occurred (in Figure 13(c)), the maximum strain was also at the ends of the pipe.

In the displacement contours (Figure 14), it can be observed that increasing the thickness will result in larger displacements. This was because displacement is also related to strain. When larger strain occurred, it would lead to larger displacements. For example, in Figure 12, it is evident that the geometry with the largest strain was geometry A-1. In Figure 13, the geometry with the largest displacement was also geometry A-1.

Apart from the aforementioned parameters, it was also necessary to know the weight of each geometry. This was an important consideration because OTEC was a hanging platform whose stability depends on the CWP. Therefore, Table 8 is the volume of geometry A-1 to A-5 to be used as a comparison of the weight of each geometry.

Table 8: Volume for D/t variable

Code	Volume (mm³)		
A-1	506.14 × 10 ⁹		
A-2	338.16 × 10 ⁹		
A-3	253.83 × 10 ⁹		
A-4	203.17 × 10 ⁹		
A-5	169.36 × 10 ⁹		

If all specimens were assumed to use the same material, then the best geometry for CWP OTEC was geometry A-5. This was because A-5 was lightweight, so it was good for CWP OTEC (can be calculated from its density). From the parameters that had been described, it can be concluded that a good geometry to use for CWP OTEC was geometry A-1. This was because geometry A-1 exhibited a significant critical moment, maximum stress, maximum strain, and maximum displacement compared to other geometries. However, this geometry also had a higher weight when compared to the other geometries.

6.2 L/D variation

The simulation results of the *L/D* variation can be seen in the moment–curvature graph in Figure 15. Figure 15 shows that the distance between stiffeners/diameter ratio had no significant effect on the magnitude of the critical moment of the structure. This was because the formula for the critical moment itself did not mention the distance between the stiffeners parameters to affect the magnitude of the critical moment (see Eqs. (3)–(5)). However, the plastic deformation region of the pipe with a shorter size was larger compared to that of the pipe with a longer size. This finding is also consistent with the discovery made by Yudo and Yoshikawa [27]. The contours can be seen in Figures 16–18.

Figure 16(a) shows the stress contours for B-1 geometry at the elastic stage (moment of 5.04×10^{10} Nmm), when entering plastic deformation (moment of 3.60×10^{12} Nmm), and at its critical moment (moment of 3.84×10^{12} Nmm). Figure 16(b) and (c) displays the stress propagation images

identical to Figure 16(a). Geometry B-3 has a critical moment of 3.72×10^{12} Nmm, while geometry B-4 has a critical moment of 3.66×10^{12} Nmm.

In Figure 16, it can be observed that the variation in L/D ratio did not significantly affect the critical stress of the structure. This was because the length did not influence the bending stress of the structure; what affects the bending stress was the cross-section of the structure. However, the stress contours differed for each L/D variation. Looking at Figure 16, it can be noted that shorter pipes had a wider spread of maximum stress on the structure. This was because in shorter pipes, failure occurred earlier before the maximum stress moved to the pipe's ends (in the tensile stress region) or toward the middle of the pipe (in the compressive stress region).

In Figure 17, it can be observed that the shorter the pipe, the higher the maximum strain in the pipe structure. This was because a shorter pipe resulted in a shorter distance between the boundary conditions and the applied load (boundary conditions can be seen in Figure 7). The close distance between the boundary conditions and the applied load caused pipes with a smaller L/D ratio to have higher maximum strain.

Figure 18 shows the displacement contours for various L/D ratios. From Figure 18, it can be observed that the longer the pipe, the larger the displacement that occurred. This was because the deflection became greater when a pipe structure was longer.

Apart from the aforementioned parameters, knowing the number of stiffeners used for each geometry was necessary. This needed to be considered because the total distance between stiffeners of the OTEC CWP could reach

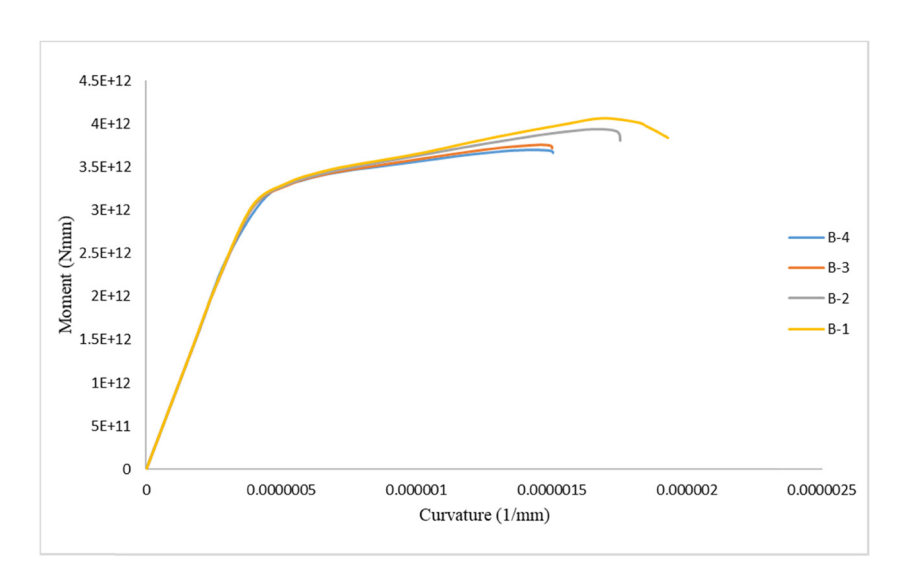


Figure 15: Moment–curvature graph for L/D variation.

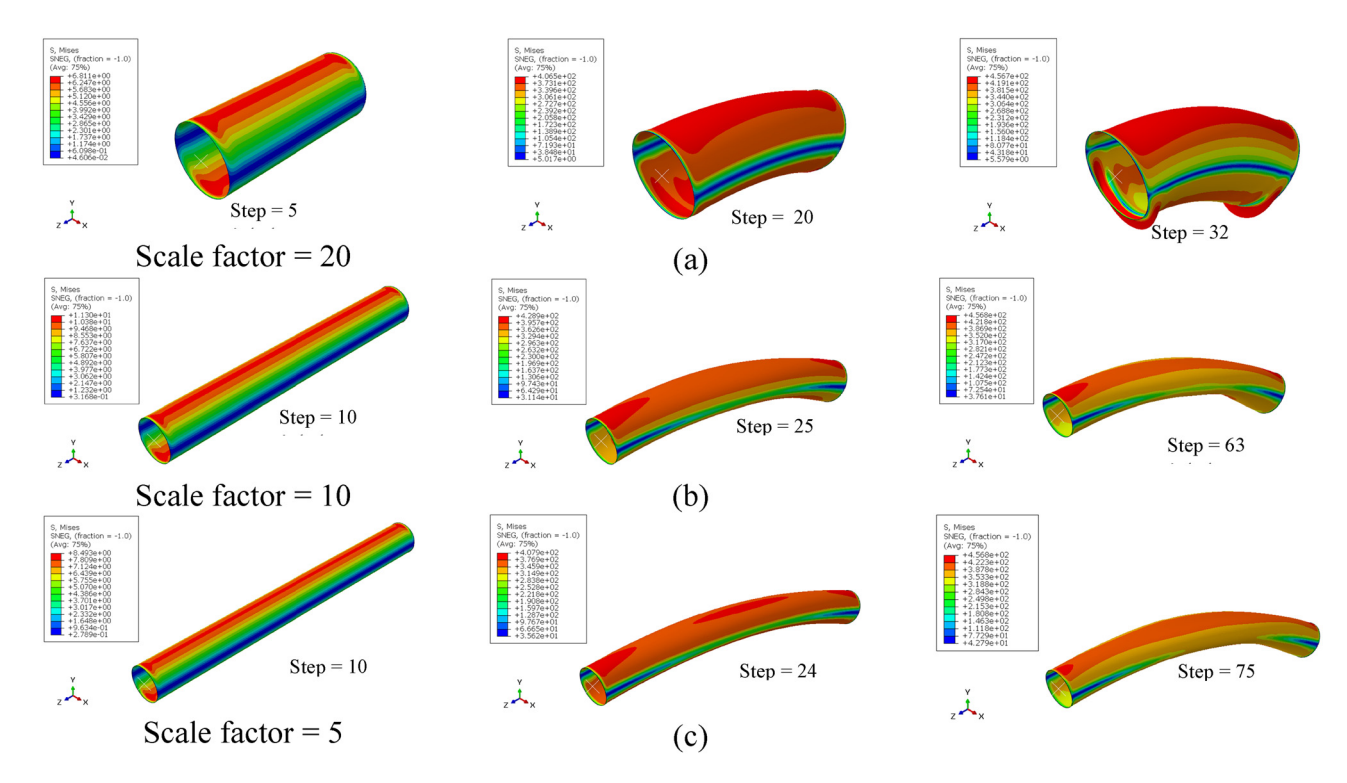


Figure 16: Stress contours: (a) B-1, (b) B-3, and (c) B-4.

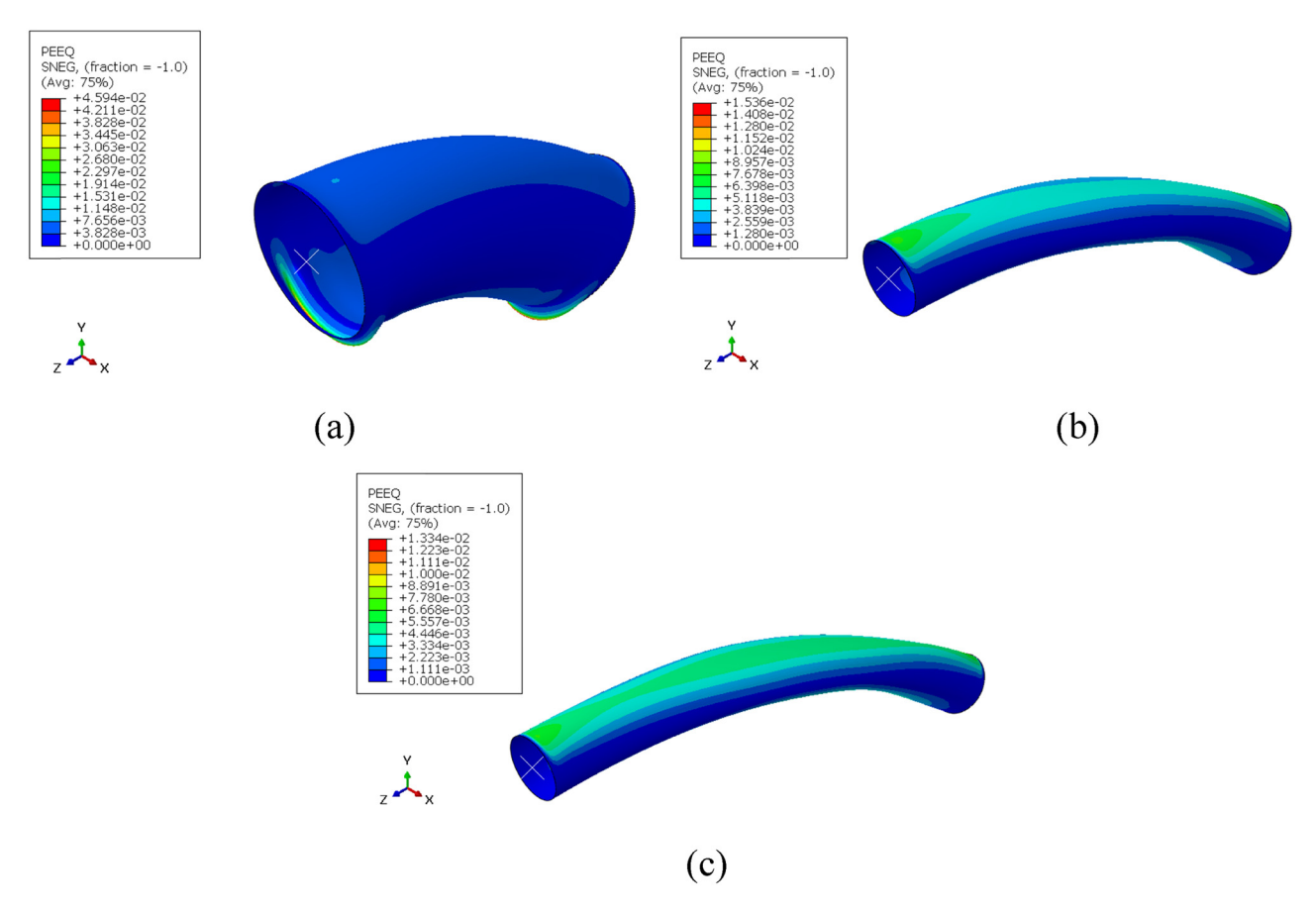


Figure 17: Strain contours: (a) B-1, (b) B-3, and (c) B-4.

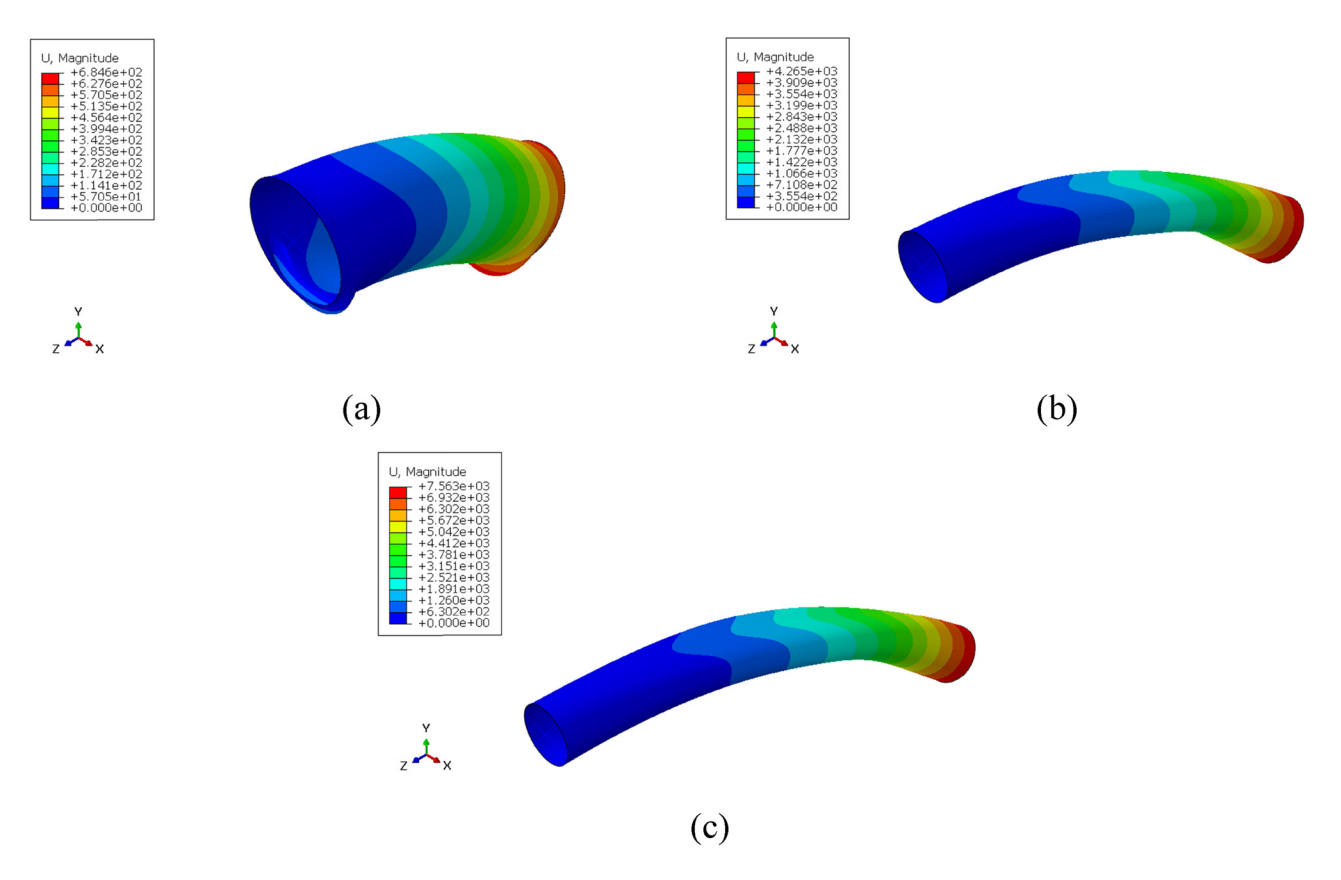


Figure 18: Displacement contours: (a) B-1, (b) B-3, and (c) B-4.

1000 m [22]. A list of the stiffeners required for each geometry can be seen in Table 9.

In Table 9, it can be seen that the greater the L/D ratio, the less stiffener was used. This shows that the B-4 geometry was a suitable geometry for CWP OTEC. With less stiffener used, costs incurred can be less. From the parameters previously described, it can be seen that the B-4 geometry was the best geometry for CWP OTEC. This was indicated by the difference in critical moment strength, which was not much different from the B-1 geometry, had a good maximum strain, and had a small number of stiffeners.

6.3 Diameter size variation

The results of the simulation of the diameter size variable can be seen in Figure 19, which is the moment–curvature graph for this variable. From the moment–curvature graph in Figure 15, it can be seen that a small diameter also had a small critical moment. Meanwhile, a large diameter had a high critical moment. This was due to the approaches to the critical moment formula in Eqs. (3)–(5), where the critical moment would also be higher when the pipe

diameter was enlarged. From the moment–curvature graph in Figure 15, it can also be seen that the smaller the diameter, the larger the plastic area.

Figure 20(a) shows the stress contours for geometry C-1 when it was still in the elastic region (moment of 8.55×10^{10} Nmm), when it entered the plastic region (moment of 9.65×10^{10} Nmm), and at its critical moment (moment of 9.73×10^{10} Nmm). Figure 20(b) and (c) displays the same stress contour changes for geometries C-2 and C-4. Geometry C-2 had a critical moment of 7.91×10^{11} Nmm, while C-4 had a critical moment of 2.68×10^{12} Nmm.

Figure 20 shows that the maximum stress of each geometry was the same. This was because each geometry's cross-section's shape was the same (D/t ratio). Despite having different diameter sizes, the critical moments of

Table 9: Amount of stiffener required

Code	Stiffener number
B-1	40
B-2	20
B-3	14
B-4	10

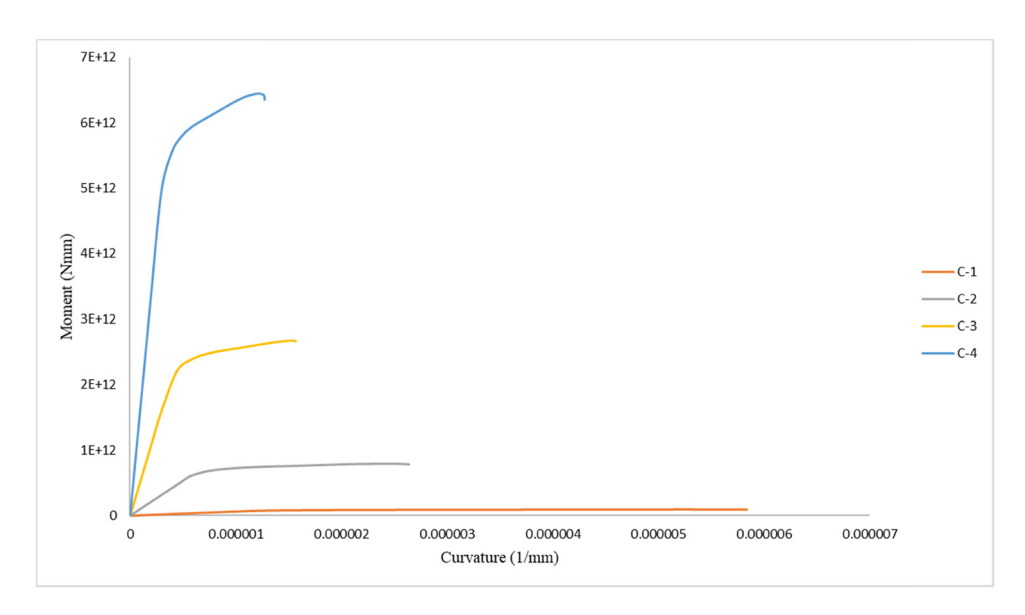


Figure 19: Moment-curvature graph for diameter size variation.

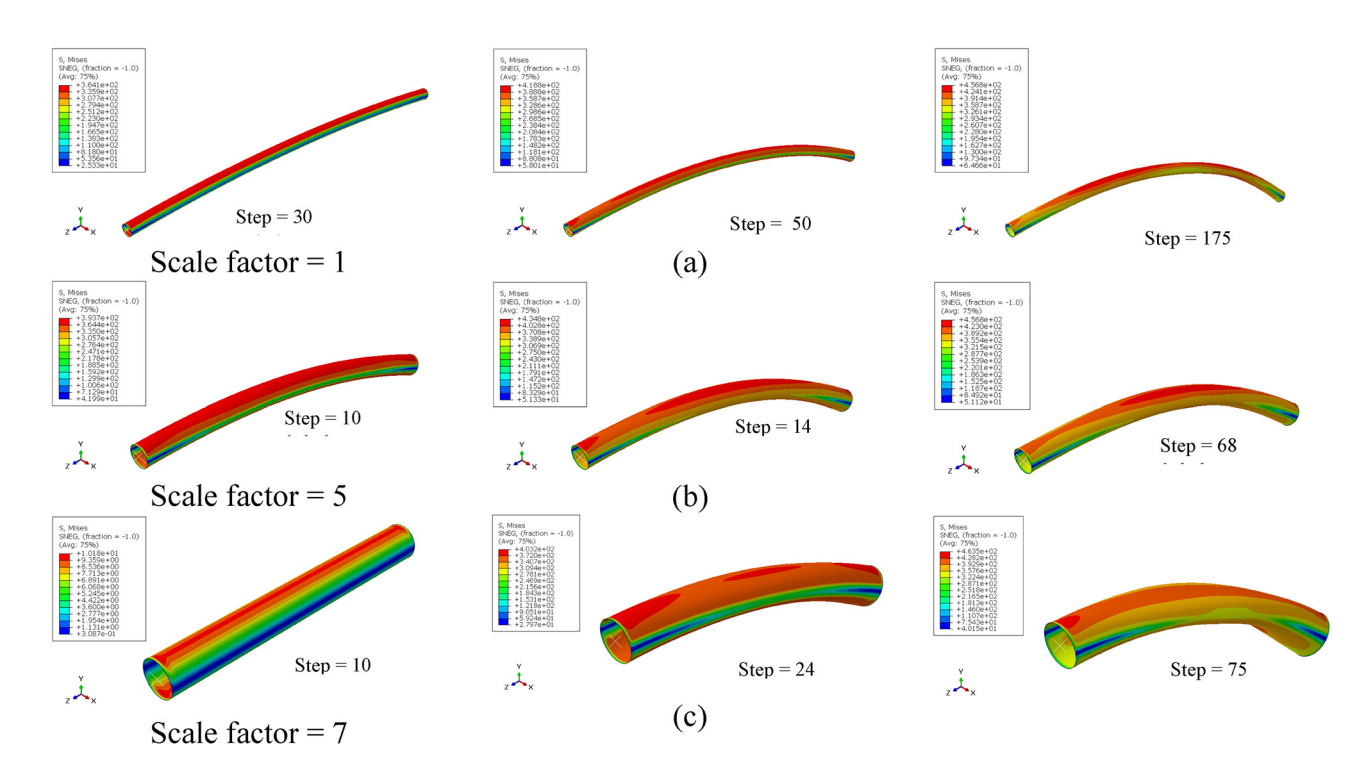


Figure 20: Stress contours: (a) C-1, (b) C-2, and (c) C-4.

each geometry were also different. This resulted in the same maximum stress for each geometry, but the sizes of the geometries were different.

In Figure 21, it can be observed that the maximum strain of the pipe structure increased as the pipe diameter was enlarged. However, even in the pipe with a 3 m diameter, it exhibited high maximum strain (in Figure 21(a)). This was because high L/D ratios tended to experience

necking, and the necking position was not at the center of the pipe. This results in necking occurred at two locations, leading to high maximum strain. The reason for necking occurred at two locations was due to the uneven load distribution along the pipe.

Figure 22 shows the displacement contours for various pipe diameter variations. It can be observed that the smaller the pipe diameter, the higher the displacement.

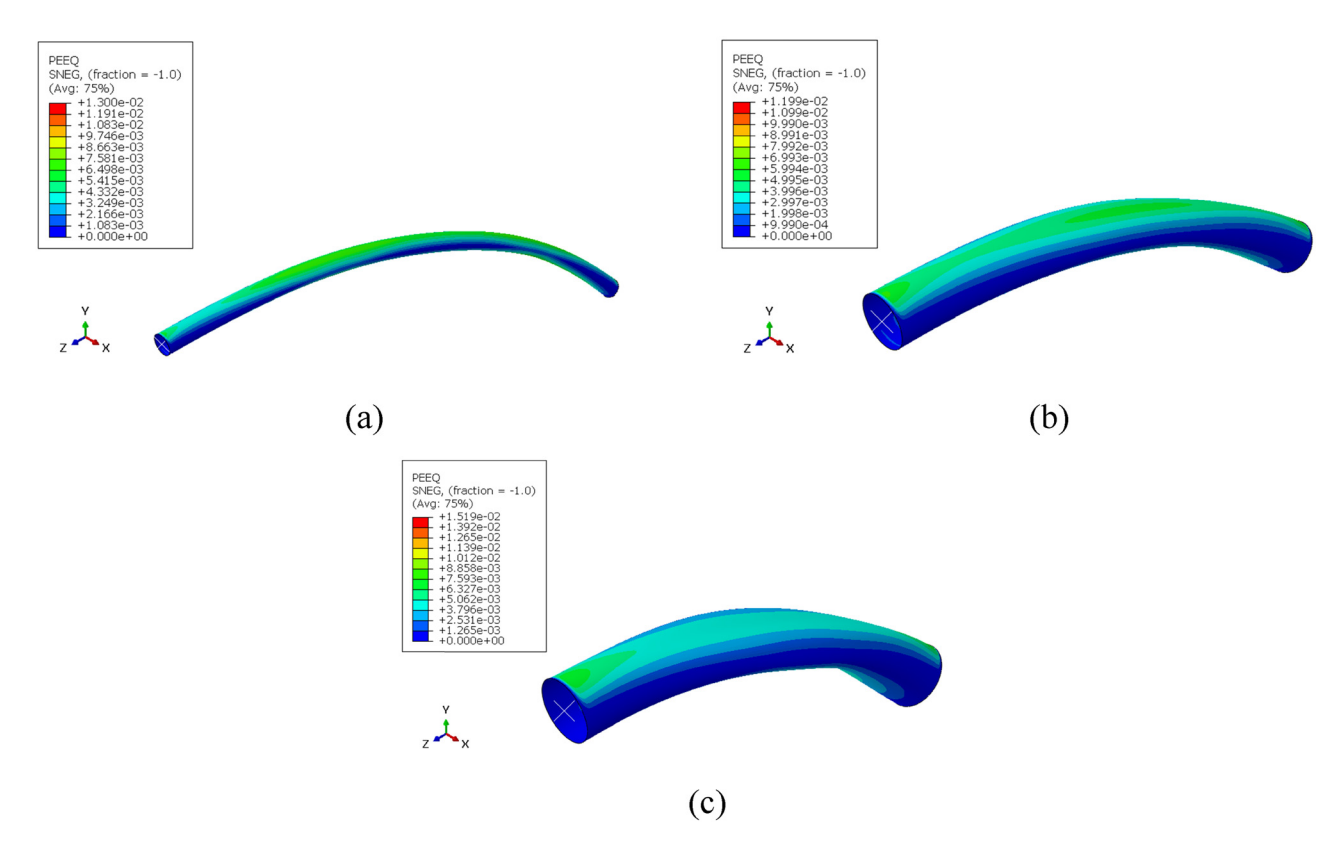


Figure 21: Strain contours: (a) C-1, (b) C-3, and (c) C-4.

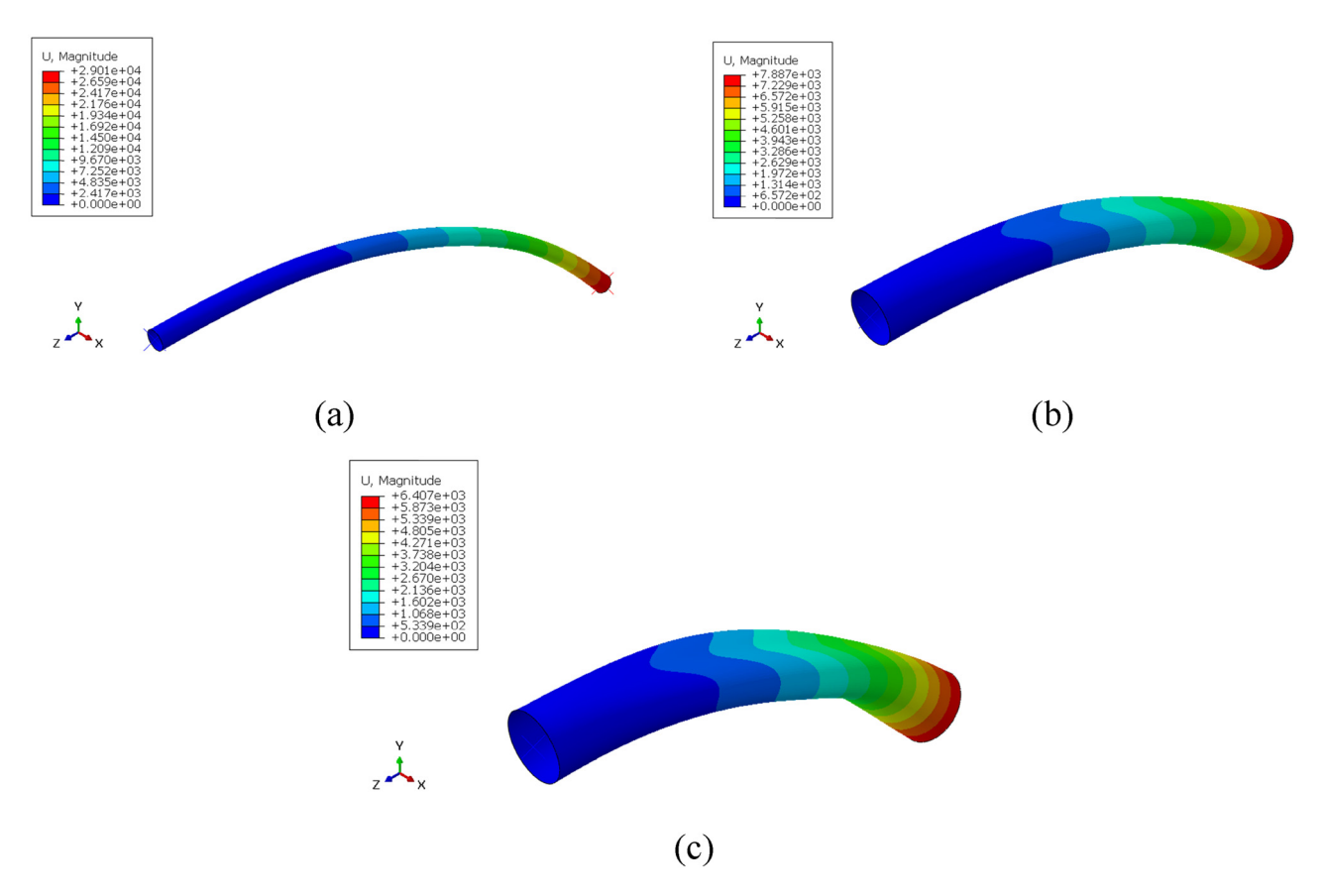


Figure 22: Displacement contours: (a) C-1, (b) C-3, and (c) C-4.

This was because as the L/D ratio increased, the displacement also increased.

When observing the moment–curvature graph, geometry C-4 had the highest critical moment compared to other geometries. However, the maximum displacement of this geometry was smaller compared to that of geometry C-1. For the selection of CWP OTEC geometry, geometry C-4 qA was chosen because the most crucial aspect of bending load Qa was its resistance to bending. Meanwhile, the maximum displacement was not as critical in its bending resistance.

6.4 Material variation

Figure 23 results from a simulation on various materials presented as a moment–curvature graph. Figure 23 shows that the material with the highest critical moment was material D-1 (steel material), followed by material D-2 and material D-3. The material belonging to the composite material had a low critical moment. The contours used can be seen in Figures 24–26.

In Figure 23, it can be observed that composite materials had low moment resistance despite having high Young's modulus and tensile strength. This was because the high tensile strength and Young's modulus resulted in significant strain. This significant strain caused the moment–curvature curve of the composite material to be elongated in its curvature (strain) region.

Figure 24(a) shows the stress contours for material D-1 when it was in the elastic region (moment of 2.72×10^{10} Nmm), when it entered the plastic region (moment of 2.61×10^{12} Nmm), and at its critical moment (moment of 2.68×10^{12} Nmm). Figure 24(b) and (c) displays the same stress contour changes for materials D-2 and D-4. The critical moment for D-2 is 1.57×10^{12} Nmm, while D-4 had a critical moment of 1.13×10^{11} Nmm.

In the stress contours (Figure 24), it was evident that the highest stress was generated by material D-1 (Figure 24(a)), while the composite material exhibited lower maximum stress (Figure 24(b)). This was because the composite's strain deformation behavior was more elongated than steel, resulting in a lower maximum stress than steel. This characteristic was also observed in the moment–curvature graph in Figure 23.

In the strain contours (Figure 25), it can be observed that the strain for the composite material was higher compared to the strain in the metallic material. This was still related to the moment–curvature graph in Figure 23. In Figure 23, the curvature that occurred in the composite material was larger than in the metallic material. This was the reason why the maximum strain in the composite material was higher than in the metallic material.

In the displacement contours (Figure 26), it can be observed that the largest displacement occurred in the composite material as well. This was because of the significant maximum strain in the composite material (Figure 25). Since a large maximum strain led to a substantial deflection

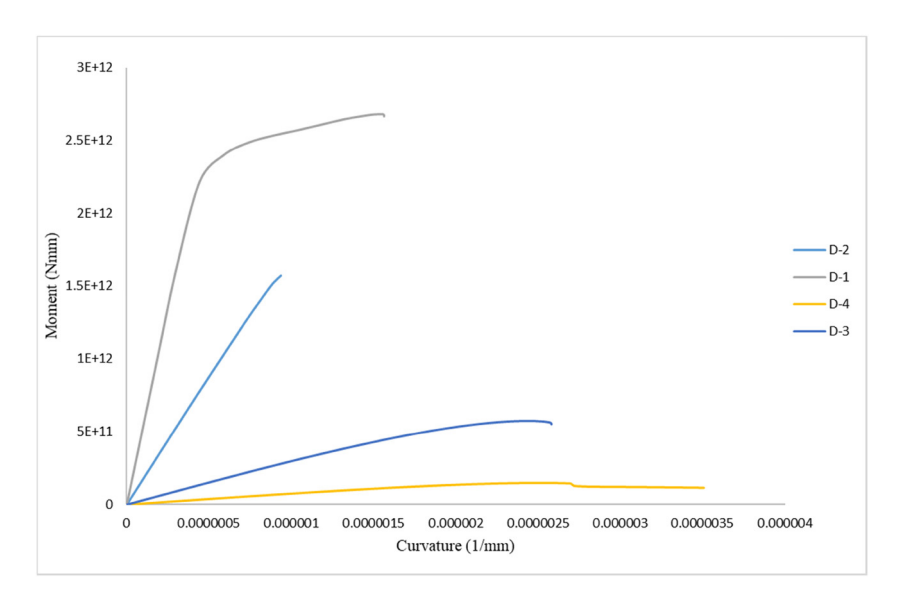


Figure 23: Moment-curvature graph for material variation.

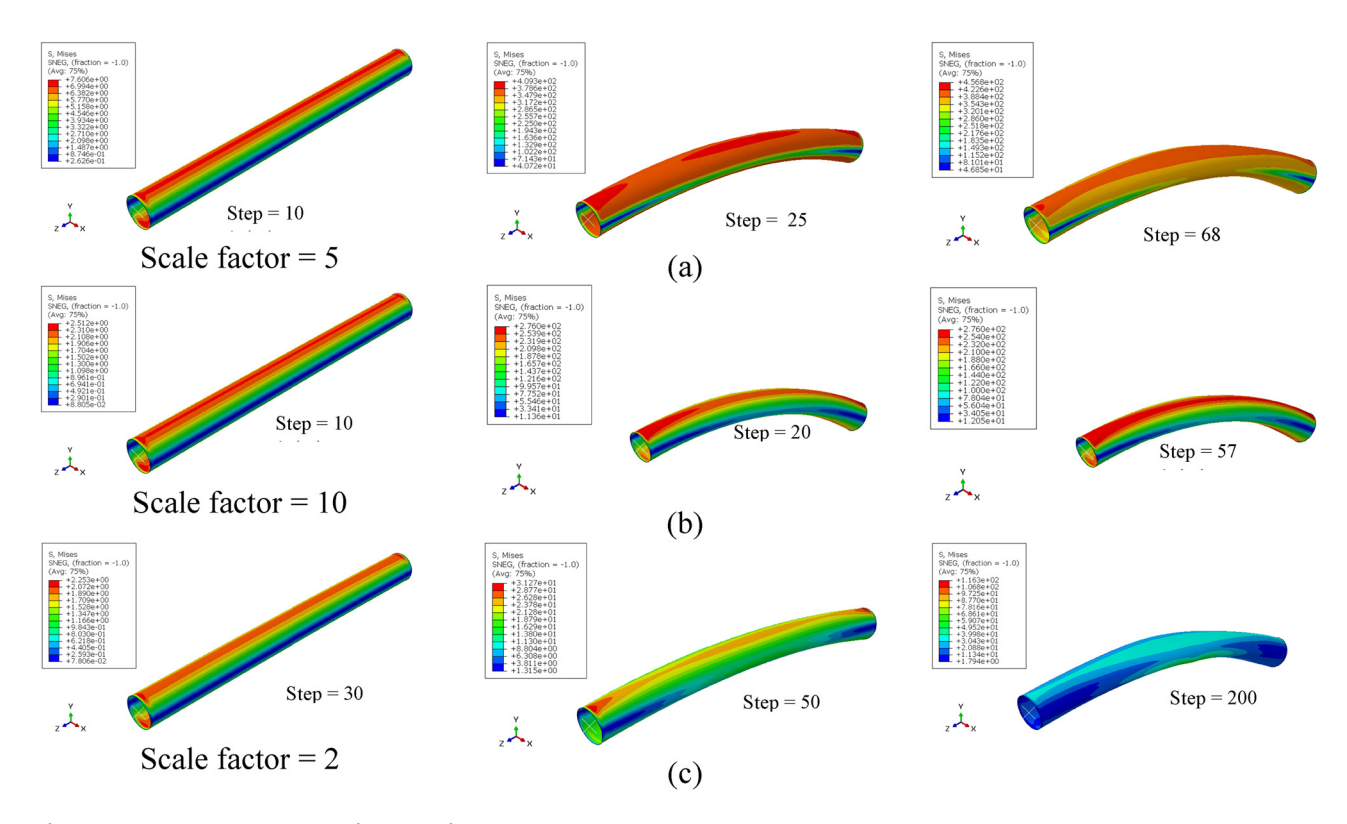


Figure 24: Stress contours: (a) D-1, (b) D-2, and (c) D-4.

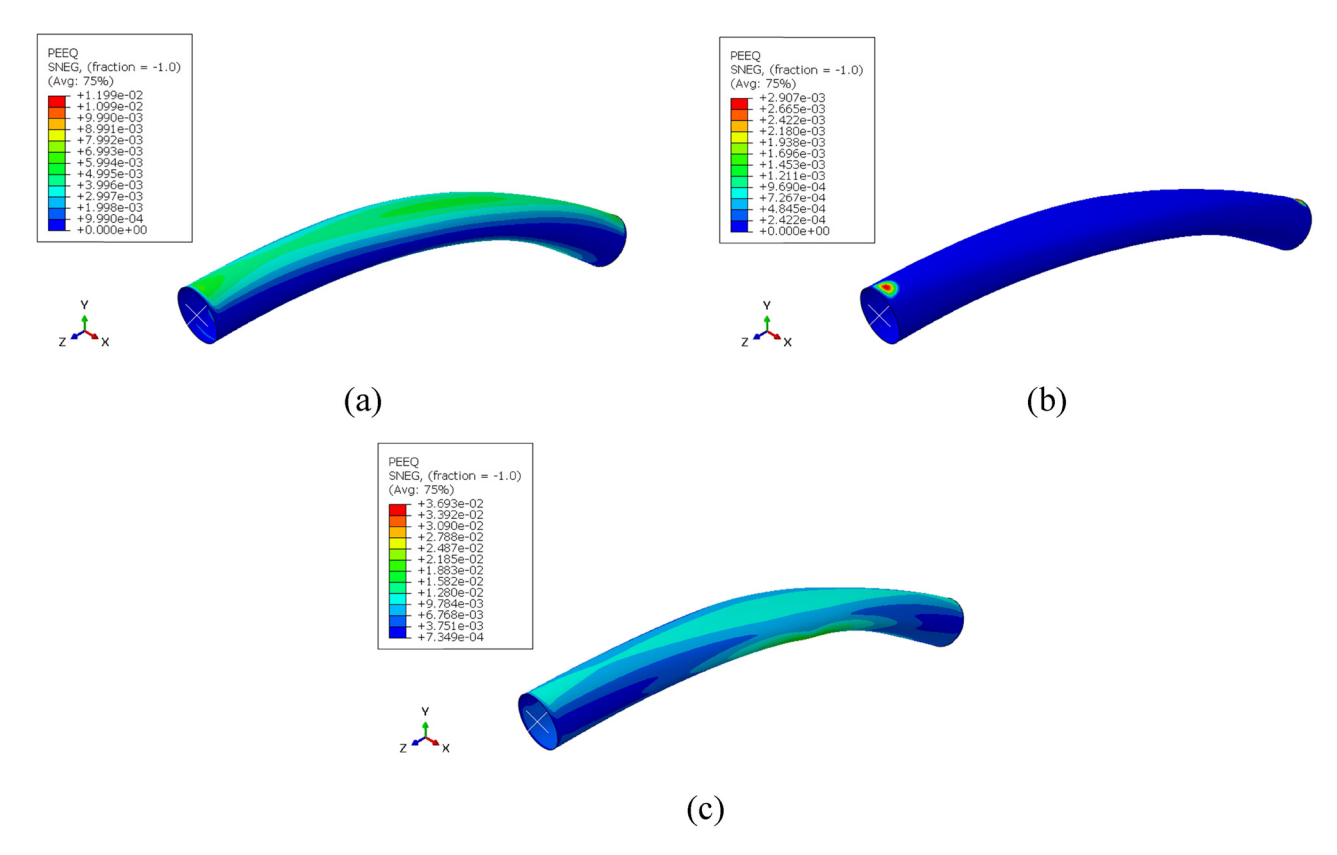


Figure 25: Strain contours: (a) D-1, (b) D-3, and (c) D-5.

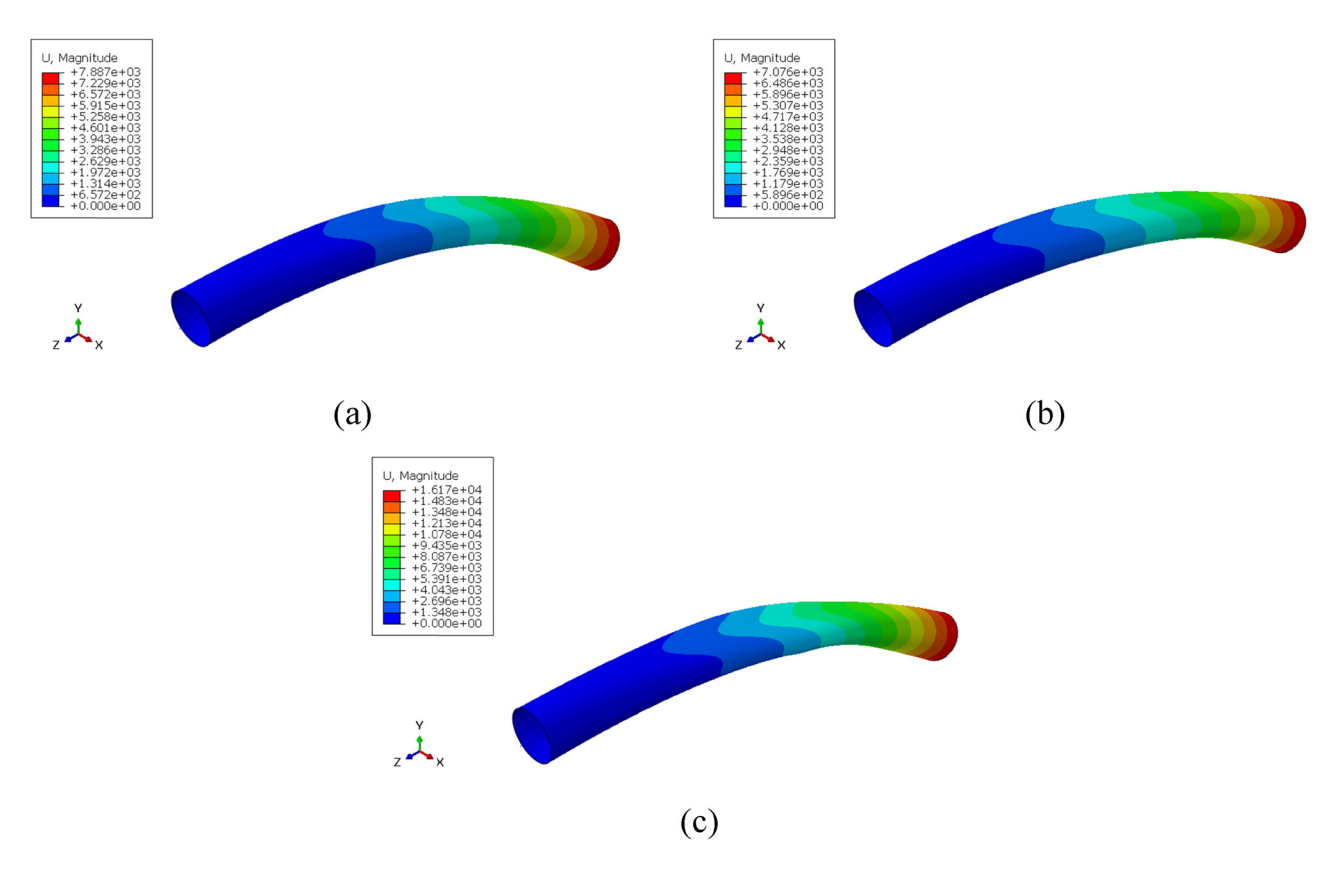


Figure 26: Displacement contours: (a) D-1, (b) D-3, and (c) D-5.

when the initial geometries were the same, the composite material exhibited the highest displacement.

In addition to the parameters discussed earlier, examining the materials' density was necessary. The density of a material affected the weight of the structure to be made. The weight would affect the balance of the OTEC floating design that will be made. Table 10 shows the materials and their density.

Suppose the geometry of the material used was assumed to be the same. In that case, the comparison of the weight of the material can be made by comparing the density of the material. It can be seen in Table 10 that the lowest material density was D-4 material, so D-4 material was the lightest in the variety of materials used. This showed that D-4 material

Table 10: Materials and their density properties

Code	Density (kg/m³)
D-1	7,840
D-2	2,700
D-3	1,800
D-4	2,500

was the best material for CWP OTEC in terms of the weight of the material used. From the previous explanations, it can be concluded that D-1 material was the best material to use for CWP OTEC. This was because the D-1 material had a very high critical moment point compared to other materials and had high maximum stress. However, this material had a relatively high weight and lower maximum strain compared to composite materials.

6.5 Imperfection variation

In the imperfection variation, the results of the simulations that had been carried out can be seen in the moment–curvature graph in Figure 27. The moment–curvature graph in Figure 27 shows that the modal shape imperfection did not affect the structure's strength even though the imperfection's size was one times the thickness of the pipe. This was because, in modal-shaped imperfections, the magnitude of the imperfections was very small and local in nature (only a small depression in the middle of the pipe). This type of imperfection would become a big problem if the multiplication factor was large.

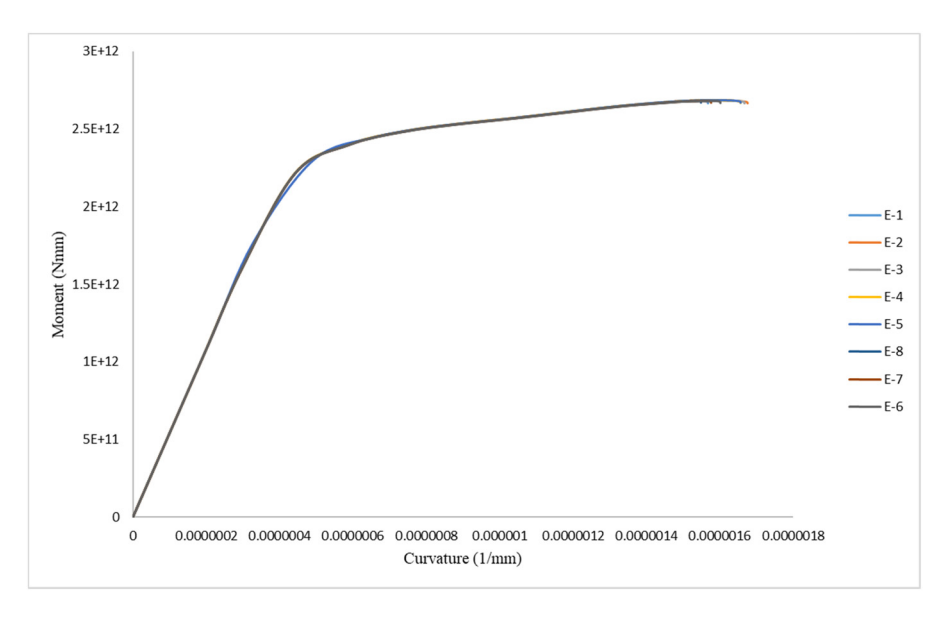


Figure 27: Moment-curvature graph for imperfection variation.

7 Conclusions

This work has successfully conducted a parametric study of CWP from OTEC installation. The finite element approach was used to calculate several designated scenarios, and the methodology in this work was validated based on pioneer work in thin steel cylindrical shells under bending. From the simulations completed, it can be concluded that:

- 1. In the variation of geometry D/t, as the D/t ratio decreased (increasing thickness), the critical moment, maximum stress, maximum strain, and maximum displacement also increased. This led to the selection of D/t geometry as 100 for the CWP OTEC.
- 2. In the variation of geometry L/D, the magnitude of the critical moment did not significantly affect the L/D ratio, resulting in only minor changes in maximum stress for each variation. However, reducing the L/D ratio (shorter pipe) increased the generated strain. On the other hand, the displacement was higher for larger L/D geometries. In this variation, an L/D value of 10 was chosen. This decision was made because this geometry exhibited a critical moment that was not significantly different from other geometries while reducing the required stiffeners.
- 3. In the variation of diameter size, it was observed that the critical moment increased with larger diameter sizes. Additionally, larger diameter sizes increased the strain due to reducing the L/D ratio. However, the strain was also high for small diameters (larger L/D ratios) because necking occurred at two points. For the diameter size variation, a diameter of 12 m was chosen as

it exhibited an exceptionally high critical moment compared to smaller sizes.

- 4. The suitable material to use when making CWP OTEC was steel material. This was because this material had a higher critical moment and maximum stress than other materials. However, this material had a relatively high weight and lower maximum strain than composite materials.
- 5. The size of the capital shape imperfection did not affect the structure of the OTEC CWP because this type of imperfection was only local.

Recommendations for subsequent research are to consider the costs in the manufacture and installation of CWP OTEC so that they can find out the geometry and materials that are more cost-efficient. In addition, it is also necessary to research combined loading between bending loading and external pressure so that the results obtained are more accurate (because CWP OTEC is under hydrostatic pressure). In addition, the future research might incorporate a heat transfer analysis in the geometry and materials used in CWP OTEC. This is due to the fact that the cold water from the deep sea must remain at a low temperature when it reaches the OTEC platform.

Funding information: This work does not involve external funding.

Author contributions: All authors have accepted responsibility for the entire content of this manuscript and approved its submission.

Conflict of interest: Aditya Rio Prabowo, who is the coauthor of this article, is a current Editorial Board member of Journal of the Mechanical Behavior of Materials. This fact did not affect the peer-review process. The authors declare no other conflict of interest.

Data availability statement: The authors declare that the data supporting the findings of this study are available within the article.

References

- Ameur HB, Han X, Liu Z, Peillex J. When did global warming start? A new baseline for carbon budgeting. Econ Model. 2022;116:106005.
- Prabowo AR, Prabowoputra DM. Investigation on Savonius turbine technology as harvesting instrument of non-fossil energy: Technical development and potential implementation. Theor Appl Mech Lett. 2020;10(4):262-9.
- Hu M, Chen S, Wang Y, Xia B, Wang S, Huang G. Identifying the key sectors for regional energy, water and carbon footprints from production-, consumption- and network-based perspectives. Sci Total Environ. 2021;764:142821.
- Yang Z, Zhang M, Liu L, Zhou D. Can renewable energy investment reduce carbon dioxide emissions? Evidence from scale and structure. Energy Econ. 2022;112:106181.
- Prabowoputra DM, Prabowo AR. Effect of Geometry Modification [5] on Turbine Performance: Mini-Review of Savonius Rotor. Int J Mech Eng Robot Res. 2022;11(10):777-83.
- Prabowoputra DM, Prabowo AR. Effect of the Phase-Shift Angle on the vertical axis Savonius wind turbine performance as a renewable-energy harvesting instrument. Energy Rep. 2022;8(Supplement 9):57-66.
- Prasetyo SD, Prabowo AR, Arifin Z. The use of a hybrid photovoltaic/ thermal (PV/T) collector system as a sustainable energy-harvest instrument in urban technology. Heliyon. 2023;9(2):e13390.
- Prabowoputra DM, Hadi S, Prabowo AR, Sohn JM. Performance investigation of the Savonius horizontal water turbine accounting for stage rotor design. Int J Mech Eng Robot Res. 2020;9(2):184-9.
- [9] Prabowoputra DM, Prabowo AR, Hadi S, Sohn JM. Assessment of turbine stages and blade numbers on modified 3D Savonius hydrokinetic turbine performance using CFD analysis. Multidiscip Model Mat Struct. 2021;17(1):253-72.
- [10] Arifin Z, Prasetyo SD, Prabowo AR, Tjahjana DDDP, Rachmanto RA. Effect of thermal collector configuration on the photovoltaic heat transfer performance with 3D CFD modeling. Open Eng. 2021;11(1):1076-85.
- [11] Arifin Z, Prasetyo SD, Tjahjana DDDP, Rachmanto RA, Prabowo AR, Alfaiz NF. The application of TiO2 nanofluids in photovoltaic thermal collector systems. Energy Rep. 2022;8(Supplement 9):1371-80.
- [12] Arifin Z, Suyitno S, Tjahjana DDDP, Juwana WE, Putra MRA, Prabowo AR. The effect of heat sink properties on solar cell cooling systems. Appl Sci. 2020;10(21):7919.
- [13] Michael E, Tjahjana DDDP, Prabowo AR. Estimating the potential of wind energy resources using Weibull parameters: A case study of the coastline region of Dar es Salaam, Tanzania. Open Eng. 2021;11(1):1093-104.
- [14] Sambodo MT, Yuliana CI, Hidayat S, Novandra R, Handoyo FW, Farandy AR, et al. Breaking barriers to low-carbon development in

- Indonesia: deployment of renewable energy. Heliyon. 2022:8(4):e09304.
- [15] Rasheed M, Mohammed OY, Shihab S, Al-Adili A. A comparative analysis of PV cell mathematical model. J Phys Conf Ser. 2021;1795(1):012042.
- [16] Abbas MM, Rasheed M. Solid state reaction synthesis and characterization of Cu doped TiO2 nanomaterials. J Phys Conf Ser. 2021:1795(1):012059.
- [17] Rasheed M, Barillé R. Room temperature deposition of ZnO and Al: ZnO ultrathin films on glass and PET substrates by DC sputtering technique. Opt Quantum Electron. 2017;49(5):1-14.
- [18] Zhang YM, Fan M, Xiao ZM, Zhang WG. The effect of surface free energy on the fracture behaviors of nanoparticle-reinforced composites. Math Mech Sol. 2023;27(3):446-61.
- [19] Alifdini I, Iskandar NAP, Nugraha AW, Sugianto DN, Wirasatriya A, Widodo AB. Analysis of ocean waves in 3 sites potential areas for renewable energy development in Indonesia. Ocean Eng. 2018;165:34-42.
- [20] Syamsuddin ML, Attamimi A, Nugraha AP, Gibran S, Afifah AQ, Oriana N. OTEC potential in the Indonesian seas. Energy Proc. 2015:65:215-22.
- [21] Yee AA. OTEC platform. Ocean Eng Oceanogr. 2015;261–80.
- [22] Adiputra R, Utsunomiya T, Koto J, Yasunaga T, Ikegami Y. Preliminary design of a 100 MW-net ocean thermal energy conversion (OTEC) power plant study case: Mentawai Island, Indonesia. J Mar Sci Technol. 2020;25(1):48-68.
- [23] Engels W, Zabihian F. Principle and Preliminary Calculation of Ocean Thermal Energy Conversion. ASEE 2014 Zone I Conference; 2014 Apr 3-5; Bridgpeort (CT), USA. ASEE, 2014.
- [24] Zhang YM, Lim CWJ, Tang C, Li B. Numerical investigation on heat transfer of melt pool and clad generation in directed energy deposition of stainless steel. Int J Therm Sci. 2021;165:106954.
- [25] Hisamatsu R, Utsunomiya T. Coupled response characteristics of cold water pipe and moored ship for floating OTEC plant. Appl Ocean Res. 2022;123:103151.
- [26] Adiputra R, Utsunomiya T. Stability based approach to design coldwater pipe (CWP) for ocean thermal energy conversion (OTEC). Appl Ocean Res. 2019;92:101921.
- [27] Yudo H, Yoshikawa T. Buckling phenomenon for straight and curved pipe under pure bending. J Mar Sci Technol. 2015;20(1):94-103.
- [28] Alshalal I, Al-Zuhairi HMI, Abtan AA, Rasheed M, Asmail MK. Characterization of wear and fatigue behavior of aluminum piston alloy using alumina nanoparticles. J Mech Behav Mater. 2023;32(1):20220280.
- [29] Zhang YM, Xiao ZM, Fan M. Fatigue investigation on railway wheel steel with white etching layer. Int J Steel Struct. 2020;20(1):80-8.
- [30] Wang Z, Yuan T, Kong X, Wu W. A universal similarity method and design procedure for buckling assessment of stiffened plates under compression load on real ships. Thin-Walled Struct. 2022:181:110025.
- [31] Li Z, Pasternak H, Jäger-Cañás A. Buckling of ring-stiffened cylindrical shell under axial compression: Experiment and numerical simulation. Thin-Walled Struct. 2021;164:107888.
- [32] Nawar MT, El-Zohairy A, Maaly HM, Husain M, Salama I, Mousa E. Prestressed steel-concrete composite I-beams with single and double corrugated web. Buildings. 2023;13(3):647.
- [33] EL Afandi M, Yehia S, Landolsi T, Qaddoumi N, Elchalakani M. Concrete-to-concrete bond Strength: A review. Constr Build Mater. 2023;363:129820.

- [34] Yu H, Guo S, Liu W, Gao R. Experimental study on stable bearing capacity of wheel-buckle formwork support frames. Structures. 2023;48:1175-89.
- [35] Ismail MS, Mahmud J, Jailani A. Buckling of an imperfect spherical shell subjected to external pressure. Ocean Eng. 2023;275:114118.
- [36] Timoshenko SP, Gere JM. Theory of elastic stability. 2nd ed. Mineola (NY), USA: Dover Publications: 2009.
- [37] Polenta V, Garvey SD, Chronopoulos D, Long AC, Morvan HP. Optimal internal pressurisation of cylindrical shells for maximising their critical bending load. Thin-Walled Struct. 2015;87:133-8.
- [38] Chwalla E. Reine Biegung schlanker, dünnwandiger Rohre mit gerader Achse. ZAMM - J Appl Math Mech. 1933;13(1):48-53.
- [39] Razier LGB. On the flexure of thin cylindrical shells and other "thin" sections. Proc R Soc Lond Ser A. 1927;116(773):104-14.
- [40] Mork J, Spiten J, Torselletti E, Ness OB, Verley R. The SUPERB project & DNV'96: buckling and collapse limit state. Proc Int Conf Offshore Mech Arct Eng. 1997;16(5):79-89.
- [41] Yin F, Shi B, Huang G, Wu X. Integrity assessment methodology of casing ovality deformation in shale gas wells. Geoenergy Sci Eng. 2023;224:211643.
- [42] Zhang T, Li L, Lu SH, Zhang JB, Zhou Z, Gong H. Effect of prestressed ultrasonic peen forming parameters on bending curvature and spherical deformation of plate. Transac Nonferrous Met Soc China. 2019;29(2):270-8.
- [43] Hutchinson J. Axial buckling of pressurized imperfect cylindrical shells. AIAA J. 2012;3(8):1461-6.
- [44] Kyriakides S, Ok A, Corona E. Localization and propagation of curvature under pure bending in steel tubes with Lüders bands. Int J Solids Struct. 2008;45(10):3074-87.
- [45] Dimopoulos CA, Gantes CJ. Experimental investigation of buckling of wind turbine tower cylindrical shells with opening and stiffening under bending. Thin-Walled Struct. 2012;54:140-55.
- [46] Ghazijahani GT, Showkati H. Experiments on cylindrical shells under pure bending and external pressure. J Constr Steel Res. 2013;88:109-22.
- [47] Karampour H, Albermani F. Buckle interaction in textured deep subsea pipelines. Ships Offshore Struct. 2015;11(6):625-35.
- [48] Yudo H, Yoshikawa T. Buckling phenomenon for imperfect pipe under pure bending. J Mar Sci Technol. 2015;29(6):703-10.
- [49] Winkler J, Georgakis CT, Fischer G. Fretting fatigue behavior of high-strength steel monostrands under bending load. Int J Fatigue. 2015;70:13-23.

- [50] Li W, Li WJ, Xu LF, Wang FC. Performance of CFDST beams using high-strength steel under bending. Structures. 2021;34:2644-55.
- **[51]** Kim SE, Papazafeiropoulos G, Truong VH, Nguyen PC, Kong Z, Duong NT, et al. Finite element simulation of normal - Strength CFDST members with shear connectors under bending loading. Eng Struct. 2021;238:112011.
- Yuan L, Zhou J, Liu H, Chen NZ. Buckling of dented bi-material pipe [52] under bending Part I: Experiments and simulation. Int J Solids Struct. 2022;257:111705.
- [53] Binazir A, Karampour H, Sadowski AJ, Gilbert BP. Pure bending of pipe-in-pipe systems. Thin-Walled Struct. 2019;145:106381.
- Sakkampang K, Sakkampang D. An experimental study and finite element analysis of the parametric of circular honevcomb core. I Mech Behav Mater. 2022:31(1):98-111.
- [55] Ridwan R, Nuriana W, Prabowo AR. Energy absorption behaviors of designed metallic square tubes under axial loading: Experimentbased benchmarking and finite element calculation. J Mech Behav Mater. 2022;31(1):443-61.
- [56] Yadav KK, Gerasimidis S. Instability of thin steel cylindrical shells under bending. Thin-Walled Struct. 2019;137:151-66.
- Zhang YM, Zhang WG, Fan M, Xiao ZM. On the mechanical beha-[57] viours of a craze in particulate-polymer composites. Philos Mag. 2018;98(15):1376-96.
- Muttagie T, Hyun Park S, Min Sohn J, Cho SR, Sik Nho I, Han S, et al. [58] Experimental investigations on the implosion characteristics of thin cylindrical aluminium-alloy tubes. Int J Solids Struct. 2020;200-201:64-82.
- Abbood IS, Odaa SA, Hasan KF, Jasim MA. Properties evaluation of [59] fiber reinforced polymers and their constituent materials used in structures - A review. Mater Today Proc. 2021;43:1003-8.
- [60] Gudonis E, Timinskas E, Gribniak V, Kaklauskas G, Arnautov AK, Tamulenas V. FRP reinforcement for concrete structures: state-ofthe-art review of application and design. Eng Struct Technol. 2014:5(4):147-58.
- [61] Cousigné O, Moncayo D, Coutellier D, Camanho P, Naceur H. Numerical modeling of nonlinearity, plasticity and damage in CFRPwoven composites for crash simulations. Compos Struct. 2014:115(1):75-88.
- [62] Bogetti TA, Hoppel CPR, Harik VM, Newill JF, Burns BP. Predicting the nonlinear response and progressive failure of composite laminates under triaxial loading: Correlation with experimental results. J Compos Mat. 2004;47(6-7):402-28.
- [63] Beer FP, Johnston ER, DeWolf JT, Mazurek DF. Statics and mechanics of materials. New York (NY), USA: McGraw-Hill Education; 2021.